Dostal, J., Martinec, Z., Thomas, M. (2012): The modelling of the toroidal magnetic field induced by tidal ocean circulation. - Geophysical Journal International, 189, 2, pp. 782—798.

DOI: http://doi.org/10.1111/j.1365-246X.2012.05407.x

Geophysical Journal International

Geophys. J. Int. (2012) **189,** 782–798 doi: 10.1111/j.1365-246X.2012.05407.x

The modelling of the toroidal magnetic field induced by tidal ocean circulation

Jan Dostal,[1] Zdeněk Martinec[2,3] and Maik Thomas[1]

[1]*Helmholtz Centre Potsdam, GFZ German Research Centre for Geosciences, Section* 1.3: *Earth System Modelling, Telegrafenberg,* D-14473, *Potsdam, Germany. E-mail: dostal@gfz-potsdam.de*

[2]*Dublin Institute for Advanced Studies,* 5 *Merrion Square, Dublin* 2, *Ireland*

[3]*Department of Geophysics, Faculty of Mathematics and Physics, Charles University in Prague, V Holešovičkách* 2, 180 00 *Prague* 8, *Czech Republic*

Accepted 2012 February 3. Received 2012 February 3; in original form 2011 May 13

SUMMARY

Observations of the ocean-induced magnetic field by the CHAMP magnetic space mission have the potential to be used as a constraint when examining ocean dynamics. This has initiated theoretical studies on the prediction of the poloidal magnetic field induced by the horizontal ocean-circulation flow. This study deals with the computation and analysis of the toroidal magnetic field induced by the tidal ocean-circulation flow on the background of the main Earth's geomagnetic field. Since the induced toroidal magnetic field cannot be modelled by the single-layer approximation model used to predict the poloidal magnetic field, we treat the ocean as a spherical layer of a finite thickness and compute the toroidal magnetic field by a matrix-propagator technique with a source of electric currents in the ocean layer.

Our numerical simulations based on the OMCT tidal ocean velocities show that the induced toroidal magnetic field is extremely sensitive to the vertical gradient of horizontal ocean flow. The larger this gradient, the stronger the induced toroidal magnetic field. Specifically, its magnitudes vary from 10^{-2} nT for barotropic flow to several nT for baroclinic flow. We show that the induced toroidal magnetic field generated by M_2 tidal forcing is comparable in amplitude to the induced poloidal part of the field. The induced toroidal and poloidal magnetic fields differ, however, in their spatial behaviour.

Key words: Numerical solutions; Tides and planetary waves; Electromagnetic theory; Geomagnetic induction; Magnetic field; Marine electromagnetics.

1 INTRODUCTION

Sea water contains a high concentration of dissolved salts. Therefore, the oceans act as an ionic fluid where the electric charges are carried by dissolved cations and anions, making sea water highly conductive. As oceans flow through the Earth's main magnetic field, the ion content in the oceans induces an electric current. As these electric currents flow around the globe, they, in turn, generate secondary magnetic fields, which evolve in terms of both magnitude and geometry through time. This effect, called motional induction, depends on the geometry and spatial scales of the ocean flow, as well as the electrical conductivity of sea water and the Earth's underlying crust and mantle (Sanford 1971).

The ocean-induced, that is motionally induced, magnetic field can be decomposed into its poloidal and toroidal components based on the Helmholtz representation of a solenoidal vector field. The poloidal magnetic field component results from toroidal electric currents flowing in horizontal planes, whereas the toroidal magnetic field component is generated by the poloidal electric currents flowing in vertical planes (e.g. Chave 1983; Chave & Luther 1990). Both magnetic fields depend on sea water transport by ocean flow, but respond in different ways to the ocean flow velocity structure. The poloidal magnetic component is predominantly sensitive to the depth integrated ocean velocities weighted by the ocean's electrical conductivity (Sanford 1971), whereas the toroidal magnetic component is largely sensitive to the vertical gradient of ocean flow velocities. The toroidal magnetic field component can only be detected inside the oceans, for example, at the seafloor, since it vanishes at the ocean surface, whereas the poloidal magnetic field component is observable outside the oceans by land observatories and satellite.

Observations of the ocean-induced magnetic field have the potential to be used as a constraint when examining ocean dynamics (Tyler *et al.* 1997b; Vivier *et al.* 2004). A number of studies have, therefore, been concerned with the forward modelling of the ocean-induced poloidal magnetic field (e.g. Sanford 1971; Chave & Luther 1990; Larsen 1992; Tyler *at al.* 1997a; Kuvshinov & Olsen 2005; Manoj *et al.* 2006). These studies predict the poloidal magnetic field induced by the horizontal ocean-circulation flow by employing a single-layer approximation

with the electrical conductivity proportional to the depth integrated ocean velocities. The predicted ocean-induced magnetic field due to the lunar semi-diurnal M_2 tide and a few other tidal waves have been validated by CHAMP satellite magnetic observations (Tyler *et al.* 2003), land-based magnetic measurements (Maus & Kuvshinov 2004) and sea surface magnetic field measurements (Lilley *et al.* 2004), despite the poloidal field being rather weak, reaching an intensity of up to a few nT.

On the other hand, the toroidal component of the ocean-induced magnetic field has been estimated to reach amplitudes of 100 nT (Sanford 1971). Since it is not *directly* observable outside the oceans, no detailed theoretical study of it has been conducted. However, interest in the motionally induced magnetic fields inside the ocean arises from the fact that seafloor geomagnetic observatories can detect electromagnetic variations associated with ocean dynamics, such as tsumani passages (Toh *et al.* 2011). In addition, the toroidal magnetic field couples with the large conductivity contrast between the oceans and continents and generates a secondary poloidal magnetic field which contributes to the poloidal magnetic field observations on land and at satellite altitudes. We may, therefore, say that the toroidal component of the ocean-induced magnetic field can *indirectly* be observed outside the oceans. In particular, a non-trivial contribution of the secondary poloidal magnetic signals to the geomagnetic field at ground-based magnetic observatories situated close to oceanic shorelines necessitates accounting for it in geomagnetic coastal-effect modelling.

This paper deals with the modelling of the toroidal magnetic field induced by ocean tidal flow. Since the toroidal magnetic field cannot be modelled by approximating the oceans by a single layer, as in the case for the poloidal magnetic field, we treat the ocean as a layer of a finite thickness. Our model assumes a spherically symmetric distribution of electrical conductivity inside the ocean and underlying earth model to make the problem tractable and obtain a first estimate of the toroidal ocean-induced magnetic field. We model the toroidal magnetic field by a matrix-propagator technique with a source of electric currents in the ocean. We perform model studies to answer the following questions. (i) What amplitude has the toroidal magnetic field induced by the M_2 tide inside the ocean? (ii) How sensitive is the M_2 induced toroidal magnetic field to the vertical gradients of ocean-flow velocities and ocean electric conductivity? (iii) What is the expected magnitude of the geomagnetic coastal effect due to the M_2 tide? and (iv) How does the underlying conducting crust and mantle affect the toroidal magnetic signal of the M_2 tide?

2 THE MOTIONALLY INDUCED MAGNETIC FIELD EQUATIONS

An electric charge q moving with ocean flow with a velocity $\boldsymbol{u}$ across the main magnetic field $\boldsymbol{B}_0$ experiences a motional electromotive force given by the magnetic force ($q\boldsymbol{u} \times \boldsymbol{B}_0$) component of the Lorentz force. This magnetic force pushes the charges through the conductive ocean and creates the electromotive force given by the electric force ($q\boldsymbol{E}$) component of the Lorentz force. In turn, this electric force induces a magnetic field $\boldsymbol{B}$. The total force exerted on an electric charge in the ocean is the sum of the motional and induced electromotive forces. The electric current generated by this force is expressed by Ohm's law for the current density $\boldsymbol{j}$

$$\boldsymbol{j} = \sigma(\boldsymbol{E} + \boldsymbol{u} \times \boldsymbol{B}_0), \tag{1}$$

where σ is the electrical conductivity of oceans. For $\boldsymbol{j}$, the form of the Maxwell's equations for the quasi-static approximation reduce to the inhomogeneous magnetic diffusion equation for the induced magnetic field $\boldsymbol{B}$:

$$\frac{1}{\mu_0}\mathrm{curl}\left(\frac{1}{\sigma}\mathrm{curl}\boldsymbol{B}\right) + \frac{\partial \boldsymbol{B}}{\partial t} = \mathrm{curl}(\boldsymbol{u} \times \boldsymbol{B}_0), \tag{2}$$

where μ_0 is the magnetic permeability of a vacuum. In the Earth's solid mantle, the motional electromotive force vanishes and the electric current density is given by the induced part only, that is $\boldsymbol{j} = \sigma\boldsymbol{E}$. The induced magnetic field, $\boldsymbol{B}$, in the mantle is then governed by a homogeneous magnetic diffusion equation.

We will be dealing with the magnetic field induced by ocean flows generated by tidal forcing with an angular frequency ω. We will assume that the ocean responds to the tidal forcing by a steady-state periodic circulation with an ocean velocity field $\boldsymbol{u}$ whose temporal variations are represented by the time-harmonic dependency $e^{i\omega t}$, that is $\boldsymbol{u}(\boldsymbol{r}, t) = \boldsymbol{u}(r)e^{i\omega t}$, where $\boldsymbol{r} = (r, \Omega)$, $\Omega = (\vartheta, \varphi)$ and $i = \sqrt{-1}$. Consequently, the induced magnetic field will be expressed in the form $\boldsymbol{B}(\boldsymbol{r}, t) = \boldsymbol{B}(r)e^{i\omega t}$.

We approximate the Earth by a conducting sphere of radius $r = a$ with a spherically symmetric distribution of electrical conductivity and divide this spherical conductor into a number of homogeneous layers, each of which is characterized by a constant electrical conductivity, σ. The magnetic diffusion equation within a homogeneous layer transforms to the Helmholtz equation

$$\nabla^2\boldsymbol{B} + k^2\boldsymbol{B} = -\mu_0\sigma\,\mathrm{curl}(\boldsymbol{u} \times \boldsymbol{B}_0), \tag{3}$$

where k is the wavenumber, $k^2 = -i\omega\mu_0\sigma$. The fundamental solution of a homogeneous Helmholtz equation is (Abramowitz & Stegun 1970)

$$\boldsymbol{B}_{\mathrm{hom}}(r, \Omega) = \sum_{jm\ell} \alpha^{\ell}_{jm} w_\ell(z) \boldsymbol{Y}^{\ell}_{jm}(\Omega), \tag{4}$$

where $z = kr$, $\boldsymbol{Y}^{\ell}_{jm}(\Omega)$ are the vector spherical harmonics (Varshalovich *et al.* 1989), and $\alpha^{\ell}_{jm} w_\ell(z)$ stands for a linear combination of the spherical Bessel functions of the 1st and 2nd kind. The summation in eq. (4) runs over $j = 1, 2, \ldots, \infty$, $m = -j, -j+1, \ldots, j$, and $\ell = j-1, j, j+1$.

To find a particular solution of the inhomogeneous Helmholtz equation (3), we denote the right-hand side of this equation by

$$\boldsymbol{F} := \mathrm{curl}(\boldsymbol{u} \times \boldsymbol{B}_0). \tag{5}$$

In Section 2.2, we will show that $\boldsymbol{F}$ can be expressed in the form

$$\boldsymbol{F}(r,\Omega)=\sum_{jm\ell}\left[{}^{(1)}F^{\ell}_{jm}\left(\frac{r}{a}\right)^{\ell}+{}^{(2)}F^{\ell}_{jm}\left(\frac{a}{r}\right)^{\ell+1}\right]\boldsymbol{Y}^{\ell}_{jm}(\Omega), \tag{6}$$

where the expansion coefficients ${}^{(1)}F^{\ell}_{jm}$ and ${}^{(2)}F^{\ell}_{jm}$ are given by eq. (35). By this, a particular solution of the inhomogeneous Helmholtz eq. (3) is searched by the ansatz

$$\boldsymbol{B}_{\rm part}(r,\Omega)=\sum_{jm\ell}\left[{}^{(1)}b^{\ell}_{jm}\left(\frac{r}{a}\right)^{\ell}+{}^{(2)}b^{\ell}_{jm}\left(\frac{a}{r}\right)^{\ell+1}\right]\boldsymbol{Y}^{\ell}_{jm}(\Omega). \tag{7}$$

Substituting the ansatz to eq. (3) and realizing that functions $r^{\ell}\boldsymbol{Y}^{\ell}_{jm}(\Omega)$ and $r^{-\ell-1}\boldsymbol{Y}^{\ell}_{jm}(\Omega)$ are harmonic, we obtain $k^2\boldsymbol{B}_{\rm part}=-\mu_0\sigma\boldsymbol{F}$, which yields the solution for the coefficients ${}^{(\alpha)}b^{\ell}_{jm}$,

$${}^{(\alpha)}b^{\ell}_{jm}=-\frac{i}{\omega}\,{}^{(\alpha)}F^{\ell}_{jm}, \tag{8}$$

$\alpha=1,2$. The complete solution of the inhomogeneous Helmholtz eq. (3) is given by the sum of a homogeneous solution $\boldsymbol{B}_{\rm hom}$, expressed by eq. (4), and the particular solution $\boldsymbol{B}_{\rm part}$, expressed by eq. (7), that is $\boldsymbol{B}=\boldsymbol{B}_{\rm hom}+\boldsymbol{B}_{\rm part}$.

To complete the specifications, boundary conditions are prescribed at spherical interfaces across which the electrical conductivity σ changes discontinuously. The continuity of the tangential components of magnetic induction and electric intensity are required (e.g. Stratton 1941):

$$\begin{aligned}\boldsymbol{e}_{\rm r}\times\left[\boldsymbol{B}\right]^{+}_{-}&=0,\\ \boldsymbol{e}_{\rm r}\times\left[\boldsymbol{E}\right]^{+}_{-}&=0,\end{aligned} \tag{9}$$

where $\boldsymbol{e}_{\rm r}$ is the unit vector in radial direction, the symbol $(f)^{+}_{-}$ indicates the jump of the quantity f at a discontinuity and the electric intensity is expressed in terms of $\boldsymbol{B}$ by Ampere's current law in the quasi-static approximation,

$$\boldsymbol{E}=\frac{1}{\mu_0\sigma}\,\mathrm{curl}\,\boldsymbol{B}. \tag{10}$$

2.1 The representation of ocean velocity $\boldsymbol{u}$ and the main magnetic field $\boldsymbol{B}_0$

To represent the source vector $\boldsymbol{F}$ in the form of a harmonic series (6), the ocean velocities $\boldsymbol{u}$ and the main magnetic field $\boldsymbol{B}_0$ need to be specified in an explicit way.

As a matter of fact, the radial component of ocean flow generated by tidal forcing is significantly smaller in comparison to the horizontal velocity components. We will, therefore, approximate the ocean flow velocity $\boldsymbol{u}$ by its horizontal components u_ϑ and u_φ,

$$\boldsymbol{u}=u_\vartheta\boldsymbol{e}_\vartheta+u_\varphi\boldsymbol{e}_\varphi, \tag{11}$$

where $\boldsymbol{e}_\vartheta$ and $\boldsymbol{e}_\varphi$ are unit base vectors in the colatitude and longitude directions, respectively. The velocity $\boldsymbol{u}$ can alternatively be represented as a series of vector spherical harmonics,

$$\boldsymbol{u}(r,\Omega)=\sum_{jm\ell}u^{\ell}_{jm}(r)\boldsymbol{Y}^{\ell}_{jm}(\Omega). \tag{12}$$

In the Appendix, we present the least-squares method for estimating the coefficients $u^{\ell}_{jm}(r)$ from gridded ocean velocities (u_ϑ,u_φ). As far as the radial dependence of $\boldsymbol{u}$ is concerned, we assume, without loss of generality, that for baroclinic flow, $\boldsymbol{u}$ is a linear function of r without a change in flow direction with depth. In the case where $\boldsymbol{u}$ is a more complex function of r, the ocean layer may be divided into a set of layers (as is the case for ocean conductivity, see Section 3.2), in each of which $\boldsymbol{u}$ can be represented as a linear function of r. Hence, we write

$$u^{\ell}_{jm}(r)=g^{\ell}_{jm}+h^{\ell}_{jm}\,r \tag{13}$$

for $r_{\rm bot}\le r\le r_{\rm top}$, where $r_{\rm top}$ and $r_{\rm bot}$ are the radii of the ocean and bottom surfaces, respectively. The coefficients g^{ℓ}_{jm} and h^{ℓ}_{jm} can be determined from a baroclinic ocean flow model.

For a background magnetic field $\boldsymbol{B}_0$, we consider the internal part of the main magnetic field of the Earth,

$$\boldsymbol{B}_0(r,\Omega)=-\sum_{j=1}^{j_{\rm main}}\sum_{m=-j}^{j}\sqrt{(j+1)(2j+1)}\left(\frac{a}{r}\right)^{j+2}G^{(i)}_{jm}\;\boldsymbol{Y}^{j+1}_{jm}(\Omega), \tag{14}$$

where $G^{(i)}_{jm}$ are the internal Gauss coefficients truncated at degree $j_{\rm main}$. To simplify the notation, we introduce

$$B^{j+1}_{0,jm}(r)=B^{j+1}_{0,jm}(a)\left(\frac{a}{r}\right)^{j+2}\quad\text{and}\quad B^{j+1}_{0,jm}(a)=-\sqrt{(j+1)(2j+1)}\,G^{(i)}_{jm}. \tag{15}$$

2.2 The representation of the source term $\boldsymbol{F}$

Having represented ocean velocity $\boldsymbol{u}$ and the main magnetic field $\boldsymbol{B}_0$ in terms of vector spherical harmonics, we aim now to express the source term $\boldsymbol{F}$ in the form of the ansatz (6). We will do this for the case when the background magnetic field $\boldsymbol{B}_0$ is characterized by *one* individual coefficient $B_{0,j_2m_2}^{j_2+1}(r)$. Hence, we assume for the moment that

$$\boldsymbol{B}_0(r,\Omega) = B_{0,j_2m_2}^{j_2+1}(r)\boldsymbol{Y}_{j_2m_2}^{j_2+1}(\Omega), \tag{16}$$

where the indexes j_2 and m_2 are fixed through the following derivation. Since the source term is linear with respect to the background magnetic field $\boldsymbol{B}_0$, the complete representation of $\boldsymbol{F}$ will be given by the sum of the representations of the individual contributions (16).

The cross-product of $\boldsymbol{u}$ and $\boldsymbol{B}_0$ reads as

$$\boldsymbol{u}\times\boldsymbol{B}_0 = \sum_{j_1m_1\ell_1} u_{j_1m_1}^{\ell_1}(r)B_{0,j_2m_2}^{j_2+1}(r)\left[\boldsymbol{Y}_{j_1m_1}^{\ell_1}(\Omega)\times\boldsymbol{Y}_{j_2m_2}^{j_2+1}(\Omega)\right], \tag{17}$$

where the cross-product of two vector spherical harmonics can be expressed as a finite sum of vector spherical harmonics (Varshalovich *et al.* 1989)

$$\boldsymbol{Y}_{j_1m_1}^{\ell_1}(\Omega)\times\boldsymbol{Y}_{j_2m_2}^{j_2+1}(\Omega) = \sum_{jm\ell} V_{j_1m_1\ell_1,j_2m_2}^{jm\ell}\boldsymbol{Y}_{jm}^{\ell}(\Omega) \tag{18}$$

with the expansion coefficients

$$V_{j_1m_1\ell_1,j_2m_2}^{jm\ell} = i\sqrt{\frac{3}{2\pi}(2j_1+1)(2j_2+1)(2\ell_1+1)(2j_2+3)}\begin{pmatrix} j_1 & \ell_1 & 1\\ j_2 & j_2+1 & 1\\ j & \ell & 1\end{pmatrix} C_{\ell_1 0 j_2+10}^{\ell 0}\, C_{j_1m_1j_2m_2}^{jm}, \tag{19}$$

where the curl brackets stand for Wigner's $9-j$ symbols and $C_{j_1m_1j_2m_2}^{jm}$ are the Clebsch–Gordan coefficients. Applying the differential operator 'curl' to eq. (17) and making use of the identity $\mathrm{curl}(f\boldsymbol{v}) = f\,\mathrm{curl}\boldsymbol{v} + \mathrm{grad}\,f\times\boldsymbol{v}$, where f and $\boldsymbol{v}$ are scalar and vector differentiable functions, respectively, we obtain

$$\begin{aligned}\mathrm{curl}(\boldsymbol{u}\times\boldsymbol{B}_0) = \sum_{j_1m_1\ell_1}\Bigg\{&u_{j_1m_1}^{\ell_1}(r)B_{0,j_2m_2}^{j_2+1}(r)\,\mathrm{curl}\left[\boldsymbol{Y}_{j_1m_1}^{\ell_1}(\Omega)\times\boldsymbol{Y}_{j_2m_2}^{j_2+1}(\Omega)\right]\\ &+\frac{d}{dr}\left[u_{j_1m_1}^{\ell_1}(r)B_{0,j_2m_2}^{j_2+1}(r)\right]\boldsymbol{e}_{\mathrm{r}}\times\left[\boldsymbol{Y}_{j_1m_1}^{\ell_1}(\Omega)\times\boldsymbol{Y}_{j_2m_2}^{j_2+1}(\Omega)\right]\Bigg\}.\end{aligned} \tag{20}$$

By eq. (18) and the relation for the 'curl' of $\boldsymbol{Y}_{jm}^{\ell}(\Omega)$ (Varshalovich *et al.* 1989),

$$\mathrm{curl}\,\boldsymbol{Y}_{jm}^{\ell}(\Omega) = \frac{1}{r}\sum_{\ell_3}\alpha_{\ell}^{\ell_3}\,\boldsymbol{Y}_{jm}^{\ell_3}(\Omega), \tag{21}$$

where the coefficients $\alpha_{\ell}^{\ell_3}$ vanish unless

$$\begin{aligned}\alpha_{j-1}^{j} &= -i\sqrt{\frac{j+1}{2j+1}}\,(j-1), \qquad \alpha_{j+1}^{j} = i\sqrt{\frac{j}{2j+1}}\,(j+2),\\ \alpha_{j}^{j-1} &= i\sqrt{\frac{j+1}{2j+1}}\,(j+1), \qquad \alpha_{j}^{j+1} = -i\sqrt{\frac{j}{2j+1}}\,(j),\end{aligned} \tag{22}$$

the first term in eq. (20) can be written as

$$\mathrm{curl}\left[\boldsymbol{Y}_{j_1m_1}^{\ell_1}(\Omega)\times\boldsymbol{Y}_{j_2m_2}^{j_2+1}(\Omega)\right] = \frac{1}{r}\sum_{jm\ell}\sum_{\ell_3} V_{j_1m_1\ell_1,j_2m_2}^{jm\ell_3}\,\alpha_{\ell_3}^{\ell}\,\boldsymbol{Y}_{jm}^{\ell}(\Omega). \tag{23}$$

Likewise, by eq. (18) and the relation for the cross-product of $\boldsymbol{e}_{\mathrm{r}}$ with $\boldsymbol{Y}_{jm}^{\ell}(\Omega)$ (Varshalovich *et al.* 1989),

$$\boldsymbol{e}_{\mathrm{r}}\times\boldsymbol{Y}_{jm}^{\ell}(\Omega) = \sum_{\ell_3}\beta_{\ell}^{\ell_3}\,\boldsymbol{Y}_{jm}^{\ell_3}(\Omega), \tag{24}$$

where the coefficients $\beta_{\ell}^{\ell_3}$ vanish unless

$$\begin{aligned}\beta_{j-1}^{j} &= \beta_{j}^{j-1} = i\sqrt{\frac{j+1}{2j+1}},\\ \beta_{j+1}^{j} &= \beta_{j}^{j+1} = i\sqrt{\frac{j}{2j+1}},\end{aligned} \tag{25}$$

we find that the second term in eq. (20) is

$$\boldsymbol{e}_{\mathrm{r}}\times\left[\boldsymbol{Y}_{j_1m_1}^{\ell_1}(\Omega)\times\boldsymbol{Y}_{j_2m_2}^{j_2+1}(\Omega)\right] = \sum_{jm\ell}\sum_{\ell_3} V_{j_1m_1\ell_1,j_2m_2}^{jm\ell_3}\,\beta_{\ell_3}^{\ell}\,\boldsymbol{Y}_{jm}^{\ell}(\Omega). \tag{26}$$

The source vector $\boldsymbol{F} = \mathrm{curl}(\boldsymbol{u} \times \boldsymbol{B}_0)$ can now be represented as a series of vector spherical harmonics

$$\boldsymbol{F}(r, \Omega) = \sum_{jm\ell} F^{\ell}_{jm}(r) \boldsymbol{Y}^{\ell}_{jm}(\Omega) \tag{27}$$

with the expansion coefficients

$$F^{\ell}_{jm}(r) = \sum_{j_1 m_1 \ell_1} \sum_{\ell_3} V^{jm\ell_3}_{j_1 m_1 \ell_1, j_2 m_2} \left\{ \alpha^{\ell}_{\ell_3} \frac{1}{r} u^{\ell_1}_{j_1 m_1}(r)\, B^{j_2+1}_{0, j_2 m_2}(r) + \beta^{\ell}_{\ell_3} \frac{d}{dr} \left[u^{\ell_1}_{j_1 m_1}(r)\, B^{j_2+1}_{0, j_2 m_2}(r) \right] \right\}. \tag{28}$$

Substituting for the radial dependence of $u^{\ell}_{jm}(r)$ and $B^{j_2+1}_{0, j_2 m_2}(r)$ from eqs (13) and (15), respectively, we find, after some algebraic manipulations, that

$$F^{\ell}_{jm}(r) = \left(D_{jm\ell, j_2 m_2} + \frac{1}{r} E_{jm\ell, j_2 m_2} \right) \left(\frac{a}{r} \right)^{j_2+2}, \tag{29}$$

where

$$\begin{aligned} D_{jm\ell, j_2 m_2} &= B^{j_2+1}_{0, j_2 m_2}(a) \sum_{j_1 m_1 \ell_1} \sum_{\ell 3} V^{jm\ell_3}_{j_1 m_1 \ell_1, j_2 m_2} \left[\alpha^{\ell}_{\ell_3} - (j_2+1) \beta^{\ell}_{\ell_3} \right] h^{\ell_1}_{j_1 m_1}, \\ E_{jm\ell, j_2 m_2} &= B^{j_2+1}_{0, j_2 m_2}(a) \sum_{j_1 m_1 \ell_1} \sum_{\ell 3} V^{jm\ell_3}_{j_1 m_1 \ell_1, j_2 m_2} \left[\alpha^{\ell}_{\ell_3} - (j_2+2) \beta^{\ell}_{\ell_3} \right] g^{\ell_1}_{j_1 m_1}. \end{aligned} \tag{30}$$

Finally, comparing the coefficients at $\boldsymbol{Y}^{\ell}_{jm}(\Omega)$ in the ansatz (6) with eq. (29), we obtain

$${}^{(1)}F^{\ell}_{jm} \left(\frac{r}{a} \right)^{\ell} + {}^{(2)}F^{\ell}_{jm} \left(\frac{a}{r} \right)^{\ell+1} = \left(D_{jm\ell, j_2 m_2} + \frac{1}{r} E_{jm\ell, j_2 m_2} \right) \left(\frac{a}{r} \right)^{j_2+2} \tag{31}$$

for all eligible indexes j, m and ℓ, but fixed indexes j_2 and m_2. The last condition should hold at any point of radius r inside the ocean layer, that is for $r_{\mathrm{bot}} \le r \le r_{\mathrm{top}}$. Considering the thickness of ocean layer being much smaller than the mean radius of the Earth, the powers $(r/a)^{\ell}$ and $(a/r)^{\ell+1}$, divided by power $(a/r)^{j_2+2}$, can be approximated within the ocean layer by $1/r$ by applying the binomial theorem,

$$\left(\frac{a}{r} \right)^{k} = \left(\frac{r+a-r}{r} \right)^{k} = \left(1 + \frac{a-r}{r} \right)^{k} = 1 + k \left(\frac{a-r}{r} \right) + O\left(\frac{a-r}{r} \right)^{2} \doteq 1 - k + k \left(\frac{a}{r} \right), \tag{32}$$

where the higher-order expansion terms can be safely neglected. In particular, for $k = -\ell - j_2 - 2$ and $k = \ell - j_2 - 1$, it holds that

$$\begin{aligned} \left(\frac{r}{a} \right)^{\ell+j_2+2} &= \ell + j_2 + 3 - (\ell + j_2 + 2) \left(\frac{a}{r} \right), \\ \left(\frac{a}{r} \right)^{\ell-j_2-1} &= -\ell + j_2 + 2 + (\ell - j_2 - 1) \left(\frac{a}{r} \right). \end{aligned} \tag{33}$$

Substituting eq. (33) into eq. (31) and comparing the constant terms and the coefficients at $1/r$, we find

$$\begin{aligned} (\ell + j_2 + 3)\, {}^{(1)}F^{\ell}_{jm} - (\ell - j_2 - 2)\, {}^{(2)}F^{\ell}_{jm} &= D_{jm\ell, j_2 m_2}, \\ -(\ell + j_2 + 2)\, {}^{(1)}F^{\ell}_{jm} + (\ell - j_2 - 1)\, {}^{(2)}F^{\ell}_{jm} &= \frac{1}{a} E_{jm\ell, j_2 m_2}. \end{aligned} \tag{34}$$

The solution of eq. (34) is, therefore,

$$\begin{aligned} {}^{(1)}F^{\ell}_{jm} &= \frac{1}{2\ell+1} \left[(\ell - j_2 - 1)\, D_{jm\ell, j_2 m_2} + (\ell - j_2 - 2) \frac{1}{a} E_{jm\ell, j_2 m_2} \right], \\ {}^{(2)}F^{\ell}_{jm} &= \frac{1}{2\ell+1} \left[(\ell + j_2 + 2)\, D_{jm\ell, j_2 m_2} + (\ell + j_2 + 3) \frac{1}{a} E_{jm\ell, j_2 m_2} \right], \end{aligned} \tag{35}$$

by which the coefficients ${}^{(\alpha)}F^{\ell}_{jm}$ of the source term $\boldsymbol{F}$ are expressed in terms of the coefficients $D_{jm\ell, j_2 m_2}$ and $E_{jm\ell, j_2 m_2}$ of $\boldsymbol{u}$ and one individual coefficient $B^{j_2+1}_{0, j_2 m_2}(a)$ of the background magnetic field $\boldsymbol{B}_0$. The complete representation of $\boldsymbol{F}$ is given by the sum of the individual contributions (35) for $j_2 = 1, \ldots, j_{\mathrm{main}}$, and $m_2 = -j_2, \ldots, j_2$.

3 MATRIX PROPAGATOR FOR THE TOROIDAL MAGNETIC FIELD

Since the aim of this paper is to compute the toroidal magnetic field induced by ocean tidal flow for a spherical approximation, and to estimate its sensitivity to the underlying ocean flow velocities, we thus confine ourselves to a toroidal magnetic source term expressed by the toroidal part of $\boldsymbol{F}$ in eq. (6),

$$\boldsymbol{F}_{\mathrm{T}}(r, \Omega) = \sum_{jm} \left[{}^{(1)}F^{j}_{jm} \left(\frac{r}{a} \right)^{j} + {}^{(2)}F^{j}_{jm} \left(\frac{a}{r} \right)^{j+1} \right] \boldsymbol{Y}^{j}_{jm}(\Omega), \tag{36}$$

where the label T stands for 'toroidal'. Since the assumed conductivity structure of the Earth is spherically symmetric and only a toroidal magnetic source is applied, the induced magnetic field is toroidal and can be expressed by the toroidal part of eqs (4), (7) and (8),

$$\boldsymbol{B}_{\mathrm{T}}(r, \Omega) = \sum_{jm} \left[\alpha^{j}_{jm} w_j(z) - \frac{i}{\omega} {}^{(1)}F^{j}_{jm} \left(\frac{r}{a} \right)^{j} - \frac{i}{\omega} {}^{(2)}F^{j}_{jm} \left(\frac{a}{r} \right)^{j+1} \right] \boldsymbol{Y}^{j}_{jm}(\Omega). \tag{37}$$

Here, the first, second and the third terms correspond to a homogeneous and two particular solutions of the Helmholtz eq. (3), respectively. The associated electric intensity, expressed by Ampere's current law (10), is a spheroidal vector field,

$$\boldsymbol{E}_{\mathrm{S}}(r,\Omega) = \frac{ik}{\mu_0\sigma}\sum_{jm}\alpha^j_{jm}\left[\sqrt{\frac{j+1}{2j+1}}\,w_{j-1}(z)\boldsymbol{Y}^{j-1}_{jm}(\Omega) - \sqrt{\frac{j}{2j+1}}\,w_{j+1}(z)\boldsymbol{Y}^{j+1}_{jm}(\Omega)\right]$$
$$+\frac{1}{\omega\mu_0\sigma\,a}\sum_{jm}\left[\sqrt{(j+1)(2j+1)}\,{}^{(1)}F^j_{jm}\left(\frac{r}{a}\right)^{j-1}\boldsymbol{Y}^{j-1}_{jm}(\Omega) - \sqrt{j(2j+1)}\,{}^{(2)}F^j_{jm}\left(\frac{a}{r}\right)^{j+2}\boldsymbol{Y}^{j+1}_{jm}(\Omega)\right]. \tag{38}$$

Furthermore, the tangential components of magnetic induction and electric intensity, required for expressing boundary conditions (9), are

$$\boldsymbol{e}_{\mathrm{r}}\times\boldsymbol{B}_{\mathrm{T}}(r,\Omega) = \sum_{jm}\left[\alpha^j_{jm}w_j(z) - \frac{i}{\omega}\,{}^{(1)}F^j_{jm}\left(\frac{r}{a}\right)^{j} - \frac{i}{\omega}\,{}^{(2)}F^j_{jm}\left(\frac{a}{r}\right)^{j+1}\right]\left(\boldsymbol{e}_{\mathrm{r}}\times\boldsymbol{Y}^j_{jm}(\Omega)\right), \tag{39}$$

$$\boldsymbol{e}_{\mathrm{r}}\times\boldsymbol{E}_{\mathrm{S}}(r,\Omega) = i\omega r\sum_{jm}\alpha^j_{jm}\frac{1}{z^2}\frac{d}{dz}\Big[zw_j(z)\Big]\boldsymbol{Y}^j_{jm}(\Omega)$$
$$+\frac{1}{k^2a}\sum_{jm}\left[(j+1)\,{}^{(1)}F^j_{jm}\left(\frac{r}{a}\right)^{j-1} - j\,{}^{(2)}F^j_{jm}\left(\frac{a}{r}\right)^{j+2}\right]\boldsymbol{Y}^j_{jm}(\Omega). \tag{40}$$

3.1 Matrix propagator for a source-free layer

We approximate the conducting Earth by a spherical conductor with a spherically symmetric electrical conductivity. We divide this spherical conductor into n homogeneous layers bounded by spheres of radii $r_1 < r_2 < \ldots < r_n = a$, where r_1 is the radius of the innermost sphere. Let the first m layers ($m < n$) approximate the solid mantle without an electric or magnetic source, while the $n - m$ upper layers approximate an ocean layer with the source electric current $\boldsymbol{j} = \sigma(\boldsymbol{u}\times\boldsymbol{B}_0)$.

Eqs (39) and (40) in a source-free layer, where ${}^{(\alpha)}F^j_{jm} = 0$, reduce to

$$\boldsymbol{e}_{\mathrm{r}}\times\boldsymbol{B}_{\mathrm{T}}(r,\Omega) = \sum_{jm}y_1(z)\Big[\boldsymbol{e}_{\mathrm{r}}\times\boldsymbol{Y}^j_{jm}(\Omega)\Big],$$
$$\boldsymbol{e}_{\mathrm{r}}\times\boldsymbol{E}_{\mathrm{S}}(r,\Omega) = i\omega r\sum_{jm}y_2(z)\boldsymbol{Y}^j_{jm}(\Omega), \tag{41}$$

where $y_1(z)$ and $y_2(z)$ are components of the 2×1 column vector $\boldsymbol{y}(z)$, which is defined as

$$\boldsymbol{y}(z) := \left\{\begin{array}{c}\alpha^j_{jm}w_j(z)\\ \alpha^j_{jm}\dfrac{1}{z^2}\dfrac{d}{dz}\Big[zw_j(z)\Big]\end{array}\right\}. \tag{42}$$

Note that the dependency of $\boldsymbol{y}(z)$ on indexes j and m is not explicitly denoted to abbreviate notations. The continuity conditions (9) then require the continuity of $\boldsymbol{y}(z)$ at spherical interfaces between homogeneous, source-free layers,

$$\big[\boldsymbol{y}(z)\big]^+_- = 0. \tag{43}$$

Recalling that $\alpha^j_{jm}w_j(z)$ stands for a linear combination of the spherical Bessel functions of the 1st and 2nd kind, $j_j(z)$ and $n_j(z)$, eq. (42) can be written in matrix form as

$$\boldsymbol{y}(z) = \boldsymbol{A}(z)\,\boldsymbol{c}, \tag{44}$$

where $\boldsymbol{c}$ is a 2×1 column vector of arbitrary constants and $\boldsymbol{A}(z)$ is the 2×2 matrix whose columns are the two fundamental solutions of the homogeneous Helmholtz equation,

$$\boldsymbol{A}(z) := \left\{\begin{array}{cc} j_j(z) & n_j(z)\\ \frac{1}{z^2}\Big[zj_j(z)\Big]' & \frac{1}{z^2}\Big[zn_j(z)\Big]'\end{array}\right\}. \tag{45}$$

Here, the prime indicates differentiation with respect to the variable z. Furthermore, the inverse matrix to $\boldsymbol{A}(z)$, needed in the following step, has the form

$$\boldsymbol{A}^{-1}(z) = z^3\left\{\begin{array}{cc}\frac{1}{z^2}\Big[zn_j(z)\Big]' & -n_j(z)\\ -\frac{1}{z^2}\Big[zj_j(z)\Big]' & j_j(z)\end{array}\right\}. \tag{46}$$

In the sth source-free layer ($s = 2, \ldots m$) with an electrical conductivity σ_s and wavenumber k_s, and bounded by radii r_{s-1} and r_s, the constants $\boldsymbol{c}$ can be eliminated by the relationship between the magnetic induction and the electric intensity at the upper and lower boundaries

of the layer:

$$\boldsymbol{y}(z_1) = \boldsymbol{B}(z_1, z_2)\boldsymbol{y}(z_2), \tag{47}$$

where $z_1 : k_s r_s$, $z_2 : k_s r_{s-1}$ and the layer propagator matrix $\boldsymbol{B}(z_1, z_2)$ can be expressed in terms of the matrix $\boldsymbol{A}$ and its inversion $\boldsymbol{A}^{-1}$ as

$$\boldsymbol{B}(z_1, z_2) := \boldsymbol{A}(z_1)\boldsymbol{A}^{-1}(z_2). \tag{48}$$

Substituting for $\boldsymbol{A}$ and $\boldsymbol{A}^{-1}$ from eqs (45) and (46), we obtain

$$\boldsymbol{B}(z_1, z_2) = z_2 \begin{bmatrix} p_j + z_2 q_j & -z_2^2 p_j \\ \frac{1}{z_1^2}(p_j + z_1 r_j + z_2 q_j + z_1 z_2 s_j) & \frac{z_2^2}{z_1^2}(-p_j - z_1 r_j) \end{bmatrix}, \tag{49}$$

where p_j, q_j, r_j and s_j are the cross-products of the spherical Bessel functions and their derivatives,

$$\begin{aligned} p_j(z_1, z_2) &:= j_j(z_1)n_j(z_2) - j_j(z_2)n_j(z_1), \\ q_j(z_1, z_2) &:= j_j(z_1)n'_j(z_2) - j'_j(z_2)n_j(z_1), \\ r_j(z_1, z_2) &:= j'_j(z_1)n_j(z_2) - j_j(z_2)n'_j(z_1), \\ s_j(z_1, z_2) &:= j'_j(z_1)n'_j(z_2) - j'_j(z_2)n'_j(z_1). \end{aligned} \tag{50}$$

The recurrence relations for the cross-products are given in Pěč *et al.* (1985).

The solution (44) in the innermost sphere ($s = 1$) must be finite at the origin, which implies that the constant in the spherical Bessel functions of the second kind must be identically equal to zero, that is, $\boldsymbol{c} = (c_1, 0)^T$. The solution for $0 \le r \le r_1$ thus takes a particular form, namely

$$\boldsymbol{y}(k_1 r) = c_1 \boldsymbol{a}(k_1 r), \tag{51}$$

where $\boldsymbol{a}(k_1 r)$ is the 2×1 column vector created from the first column of matrix $\boldsymbol{A}(z)$ and divided by $j_j(k_1 r_1)$ for numerical convenience. The solution in the sth spherical layer then follows from the upward continuation of the solution from the innermost sphere and the continuity condition (43) of $\boldsymbol{y}(z)$ at the interfaces at $r_1 \ldots r_m$. This corresponds to the multiplication of the product of the layer propagator matrices with the inner sphere solution taken at $r = r_1$. In the sth layer, ($r_{s-1} \le r \le r_s$, $s = 2, \ldots, m$), we obtain

$$\boldsymbol{y}(k_s r) = \boldsymbol{L}(k_s r, k_1 r_1)\boldsymbol{y}(k_1 r_1), \tag{52}$$

where

$$\boldsymbol{L}(k_s r, k_1 r_1) = \boldsymbol{B}(k_s r, k_s r_{s-1})\boldsymbol{B}(k_{s-1} r_{s-1}, k_{s-1} r_{s-2}) \ldots \boldsymbol{B}(k_2 r_2, k_2 r_1). \tag{53}$$

Substituting for $\boldsymbol{y}(k_1 r_1)$ from eq. (51), we have

$$\boldsymbol{y}(k_s r) = c_1 \boldsymbol{L}(k_s r, k_1 r_1)\boldsymbol{a}(k_1 r_1), \tag{54}$$

where

$$\boldsymbol{a}(k_1 r_1) = \begin{Bmatrix} 1 \\ \frac{1}{k_1^2 r_1^2}\left[j + 1 - \chi_j(k_1 r_1)\right] \end{Bmatrix}, \tag{55}$$

and $\chi_j(z) : z j_{j+1}(z)/j_j(z)$. The recurrence relation for function $\chi_j(z)$ is given in Pěč *et al.* (1985).

3.2 Matrix propagator for the ocean layer

The uppermost layers, labelled by $m + 1$, $m + 2$, …, n, and bounded by spheres of radii r_{m+1}, r_{m+2}, …, r_n, approximate an ocean layer with electrical conductivities σ_{m+1}, σ_{m+2}, …, σ_n, and with the source electric current $\boldsymbol{j}_s = \sigma_s(\boldsymbol{u} \times \boldsymbol{B}_0)$, $s = m + 1, m + 2, \ldots, n$. Note that ocean velocity $\boldsymbol{u}$ and the main magnetic field $\boldsymbol{B}_0$ are not labelled by the layer index s since both are assumed to be continuous functions of a position in the entire ocean layer (see Section 2.1).

The magnetic induction and the electric intensity within the sth ocean layer are given by eqs (39) and (40). To express them in a shorter form, we introduce the 2×1 column source-term vector

$$\boldsymbol{s}_s(r) := -\frac{i}{\omega} \begin{Bmatrix} {}^{(1)}F^j_{jm}\left(\frac{r}{a}\right)^j + {}^{(2)}F^j_{jm}\left(\frac{a}{r}\right)^{j+1} \\ \frac{1}{k_s^2 a^2}\left[(j+1)\,{}^{(1)}F^j_{jm}\left(\frac{r}{a}\right)^{j-2} - j\,{}^{(2)}F^j_{jm}\left(\frac{a}{r}\right)^{j+3}\right] \end{Bmatrix}, \tag{56}$$

where $r_{s-1} \le r \le r_s$, $s = m + 1, m + 2, \ldots, n$ and the dependency of $\boldsymbol{s}_s(r)$ on indexes j and m is not explicitly denoted. Then, eqs (39) and

(40) in the sth source layer can be written in an analogous form as eq. (41) for a source-free layer,

$$\begin{aligned} \boldsymbol{e}_{\mathrm{r}} \times \boldsymbol{B}_{\mathrm{T}}(r, \Omega) &= \sum_{jm} v_1(r)\Big[\boldsymbol{e}_{\mathrm{r}} \times \boldsymbol{Y}^{j}_{jm}(\Omega)\Big], \\ \boldsymbol{e}_{\mathrm{r}} \times \boldsymbol{E}_{\mathrm{S}}(r, \Omega) &= i\omega r \sum_{jm} v_2(r)\boldsymbol{Y}^{j}_{jm}(\Omega), \end{aligned} \tag{57}$$

where $v_1(r)$ and $v_2(r)$ are components of the 2×1 column vector $\boldsymbol{v}(r)$ expressed as

$$\boldsymbol{v}(r) = \boldsymbol{A}(k_s r)\boldsymbol{c}_s + \boldsymbol{s}_s(r). \tag{58}$$

Here, the matrix $\boldsymbol{A}(z)$ is given by eq. (45), k_s is the wavenumber for the sth ocean-layer parameters and $\boldsymbol{c}_s$ is a 2×1 column vector with arbitrary constants. The unknown constants $\boldsymbol{c}_s$ in eq. (58) can be eliminated by the values of magnetic induction and the electric intensity taken at the bottom ($r = r_{s-1}$) of the sth layer:

$$\boldsymbol{v}(r_{s-1}) = \boldsymbol{A}(k_s r_{s-1})\boldsymbol{c}_s + \boldsymbol{s}_s(r_{s-1}), \tag{59}$$

which yields

$$\boldsymbol{c}_s = \boldsymbol{A}^{-1}(k_s r_{s-1})[\boldsymbol{v}(r_{s-1}) - \boldsymbol{s}_s(r_{s-1})]. \tag{60}$$

The solution in the sth ocean layer for $r_{s-1} \le r \le r_s$ is then

$$\boldsymbol{v}(r) = \boldsymbol{B}(k_s r, k_s r_{s-1})[\boldsymbol{v}(r_{s-1}) - \boldsymbol{s}_s(r_{s-1})] + \boldsymbol{s}_s(r), \tag{61}$$

where the matrix $\boldsymbol{B}$ is provided by eq. (49).

The continuity conditions (9) require the continuity of $\boldsymbol{v}(r)$ at spherical interfaces between homogeneous ocean source layers,

$$\big[\boldsymbol{v}(r)\big]^{+}_{-} = 0. \tag{62}$$

To make use of this condition, let us consider the solution in the two innermost ocean layers, labelled by indexes $s = m + 1$ and $s = m + 2$, taken at radii r_{m+1} and $r_{m+1} \le r \le r_{m+2}$, respectively,

$$\begin{aligned} \boldsymbol{v}(r_{m+1}) &= \boldsymbol{B}(k_{m+1} r_{m+1}, k_{m+1} r_m)[\boldsymbol{v}(r_m) - \boldsymbol{s}_{m+1}(r_m)] + \boldsymbol{s}_{m+1}(r_{m+1}), \\ \boldsymbol{v}(r) \quad &= \boldsymbol{B}(k_{m+2} r, k_{m+2} r_{m+1})[\boldsymbol{v}(r_{m+1}) - \boldsymbol{s}_{m+2}(r_{m+1})] + \boldsymbol{s}_{m+2}(r). \end{aligned} \tag{63}$$

By the continuity condition (62) taken at the interface $r = r_{m+1}$, the last two equations can be combined such that $\boldsymbol{v}(r_{m+1})$ is eliminated,

$$\begin{aligned} \boldsymbol{v}(r) = {} & \boldsymbol{L}(k_{m+2} r, k_{m+1} r_m)[\boldsymbol{v}(r_m) - \boldsymbol{s}_{m+1}(r_m)] \\ & + \boldsymbol{L}(k_{m+2} r, k_{m+2} r_{m+1})[\boldsymbol{s}_{m+1}(r_{m+1}) - \boldsymbol{s}_{m+2}(r_{m+1})] + \boldsymbol{s}_{m+2}(r), \end{aligned} \tag{64}$$

where matrix $\boldsymbol{L}(k_{m+2} r, k_{m+1} r_m)$ is given by eq. (53) and $\boldsymbol{L}(k_{m+2} r, k_{m+2} r_{m+1}) \equiv \boldsymbol{B}(k_{m+2} r, k_{m+2} r_{m+1})$.

The procedure continues successively. The solution in the sth ocean layer, $s = m + 3, \ldots, n$, then follows from the upward continuation of the solution (64) in the $(m + 2)$th ocean layer and the continuity condition (62) at the interface $r = r_{m+2}, \ldots, r_n$. In the sth layer, that is for $r_{s-1} \le r \le r_s$, we obtain

$$\begin{aligned} \boldsymbol{v}(r) = {} & \boldsymbol{L}(k_s r, k_{m+1} r_m)[\boldsymbol{v}(r_m) - \boldsymbol{s}_{m+1}(r_m)] \\ & + \boldsymbol{L}(k_s r, k_{m+2} r_{m+1})[\boldsymbol{s}_{m+1}(r_{m+1}) - \boldsymbol{s}_{m+2}(r_{m+1})] \\ & + \ldots \\ & + \boldsymbol{L}(k_s r, k_s r_{s-1})[\boldsymbol{s}_{s-1}(r_{s-1}) - \boldsymbol{s}_s(r_{s-1})] + \boldsymbol{s}_s(r). \end{aligned} \tag{65}$$

The continuity conditions (9) require the continuity of the tangential components of the magnetic induction and the electrical intensity at the ocean-bottom–solid mantle interface,

$$\boldsymbol{y}(k_m r_m) = \boldsymbol{v}(r_m). \tag{66}$$

Substituting for $\boldsymbol{y}(k_m r_m)$ from eq. (54) and then entering this result into eq. (65), we obtain

$$\begin{aligned} \boldsymbol{v}(r) = {} & \boldsymbol{L}(k_s r, k_{m+1} r_m)[c_1 \boldsymbol{L}(k_m r_m, k_1 r_1)\boldsymbol{a}(k_1 r_1) - \boldsymbol{s}_{m+1}(r_m)] \\ & + \boldsymbol{L}(k_s r, k_{m+2} r_{m+1})[\boldsymbol{s}_{m+1}(r_{m+1}) - \boldsymbol{s}_{m+2}(r_{m+1})] \\ & + \ldots \\ & + \boldsymbol{L}(k_s r, k_s r_{s-1})[\boldsymbol{s}_{s-1}(r_{s-1}) - \boldsymbol{s}_s(r_{s-1})] + \boldsymbol{s}_s(r). \end{aligned} \tag{67}$$

Finally, the toroidal magnetic field at the Earth's surface must vanish, that is $v_1(r_n) = 0$, which gives the equation for unknown constant c_1,

$$c_1 = \frac{1}{\left\{\boldsymbol{L}(k_n r_n, k_1 r_1)\boldsymbol{z}(k_1 r_1\right]_1} \Big\{ \boldsymbol{L}(k_n r_n, k_{m+1} r_m)\boldsymbol{s}_{m+1}(r_m) - \boldsymbol{L}(k_n r_n, k_{m+2} r_{m+1})[\boldsymbol{s}_{m+1}(r_{m+1}) - \boldsymbol{s}_{m+2}(r_{m+1})] - \ldots - \boldsymbol{L}(k_n r_n, k_n r_{n-1})[\boldsymbol{s}_{n-1}(r_{n-1}) - \boldsymbol{s}_n(r_{n-1})] - \boldsymbol{s}_n(r_n) \Big\}_1 , \tag{68}$$

where $\left(\boldsymbol{a}\right)_1$ denotes the first component of vector $\boldsymbol{a}$.

In summary, the solution $\boldsymbol{y}(k_s r)$ in the sth source-free layer, $r_{s-1} \le r \le r_s$, $s = 2, \ldots, m$, is expressed by eq. (54) with the constant c_1 given by eq. (68). The solution $\boldsymbol{v}(r)$ in the sth ocean layer, $r_{s-1} \le r \le r_s$, $s = m+1, \ldots, n$, is given by eq. (65) with $\boldsymbol{v}(r_m)$ given by eq. (66).

4 INPUT DATA

4.1 Ocean velocities

The input ocean velocities are generated by the ocean model for circulation and tides (OMCT; Thomas 2002; Dobslaw & Thomas 2007) over a regular (ϑ, φ) grid with a size of 1.875° in latitude and longitude. In our calculations, we use the barotropic (vertically averaged velocities) ocean circulation flow of the lunar semi-diurnal tide M_2 with a period of 12 hr and 42 min. The strong M_2 tidal wave induces large ocean velocities in shallow-water coastal regions, which is particularly important for the induced toroidal magnetic field. To account for this effect, we choose the thickness of the ocean layer to equal 1 km.

The least-squares method (presented in the Appendix) is then applied to the gridded ocean velocities $(u^i_\vartheta, u^i_\varphi)$ to compute the least-squares estimate $\hat{u}^\ell_{jm}$ of the spherical harmonic expansion coefficients u^ℓ_{jm} of horizontal ocean velocity $\boldsymbol{u}$. For a grid-step size of 1.875°, the angular degree $j = 95$ is the highest degree for which the discrete velocity data can unambiguously be the represented by spherical harmonic series in eq. (12). To achieve a reliable result, we represent the ocean velocity by the vector spherical harmonic series eq. (12) cut-off at degree $j_{\max} = 48$. In addition, to mitigate the effect of the Gibbs phenomenon, the series in eq. (12) is weighted by the Lanczos η_j coefficients (Duchon 1979). In summary, the input horizontal ocean velocities are represented in the form

$$\boldsymbol{u}(r, \vartheta, \varphi) = \sum_{j=1}^{j_{\max}} \sum_{m=-j}^{j} \sum_{\ell=j-1}^{j+1} \eta_j \, \hat{u}^\ell_{jm}(r) \boldsymbol{Y}^\ell_{jm}(\vartheta, \varphi). \tag{69}$$

Fig. 1 shows the real and imaginary parts of the ϑ and φ components of the ocean velocities synthesized from the spherical harmonics coefficients $\hat{u}^\ell_{jm}$, according to eq. (69). We can see large-scale spatial patterns in the ocean velocities over deep-water open oceans and rather short-wavelength spatial patterns over shallow-water coastal regions. Due to the truncation of the spherical harmonic series in eq. (69), the modelled ocean velocities slightly overlap continental coastal regions. This will not, however, affect our estimates of the size and scale of the induced toroidal magnetic field, but it would be a limitation when the observed magnetic field is interpreted in terms of ocean velocities.

4.2 Electrical conductivity model

The spherically symmetric earth conductivity model consists of two parts, the ocean where the sea currents induce the secondary magnetic field (in this paper, we only consider its toroidal component) and the source-free layers beneath the seafloor. We divide the ocean into six spherical layers where electrical conductivity varies piecewise uniformly from 4.7 S m^{-1} at the sea surface to 3.2 S m^{-1} at the ocean bottom due to varying water temperature. The conductivity of the underlying sediments, lithosphere and mantle is divided into 19 layers with different thicknesses (see Fig. 2) and follows, up to a large extent, the model proposed by Lizarralde *et al.* (1995) and Baba *et al.* (2010) for the Northeastern Pacific mantle conductivity profile. The conductivity of the top, 4-km thick sedimentary layer is set equal to 0.3 S m^{-1}. Underneath this layer, the conductivity gradually decreases to 0.001 S m^{-1} at a depth of 50 km. Then, the conductivity increases to 0.05 S m^{-1} until a depth of 250 km. Below this maximum, the conductivity slightly decreases to 0.03 S m^{-1} at 380 km. Finally, the conductivity at the top of the lower mantle is equal 1 S m^{-1} and is fixed at this rate downwards, since its effect on the induced magnetic field is negligible (see the next section).

5 NUMERICAL RESULTS

To estimate a possible range of magnitudes and spatial behaviour of the induced toroidal magnetic field, we consider two limiting cases for the radial profile of horizontal ocean velocities. Most commonly, the tidally induced ocean circulation is approximated by a barotropic flow where ocean velocities are considered constant throughout a sea water column. If a barotropic flow is circulating in a square box within the (x, y) plane under a homogeneous background magnetic field with a non-zero vertical component, the toroidal magnetic field will not be induced. However, due to the spherical geometry of the ocean layer, a barotropic ocean flow in a spherical layer induces a toroidal magnetic field. Fig. 3 shows the ϑ and φ components of the toroidal magnetic field at the ocean bottom for a barotropic ocean flow. As expected from

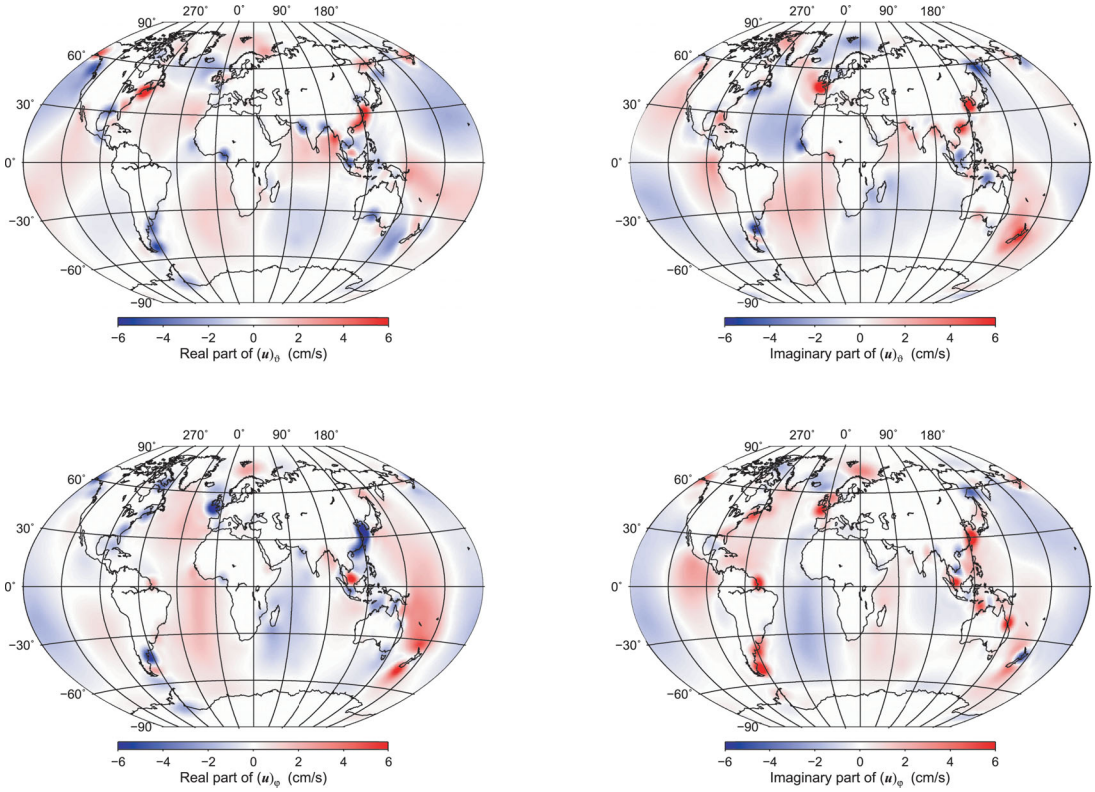

Figure 1. Real (left) and imaginary (right) parts of the ϑ (top) and φ (bottom) components of the barotropic ocean velocities for the M_2 tide synthesized from the spherical harmonics coefficients $\hat{u}^{\ell}_{jm}$.

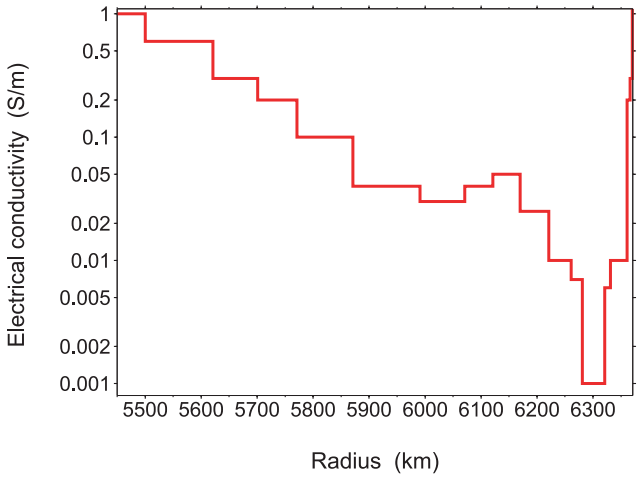

Figure 2. Radial profile of electrical conductivity (in S m^{-1}) beneath the ocean layer.

the square box analogue, the field is small in amplitude, reaching its maximum values at the ocean bottom of about ± 0.003 nT in coastal regions.

In the second case, we consider that the ocean flow is not exactly barotropic, but has a baroclinic component by assuming that the magnitude (not the direction) of the ocean velocities vary with ocean depth. The model in eq. (13) of ocean velocities is intentionally designed to enable a linear change of ocean velocity with depth. We will consider the maximum linear gradient of ocean flow such that the velocities are set equal to the input OMCT ocean velocities at the top of ocean layer and vanish at the ocean bottom. Fig. 4 shows the ϑ and φ components of the toroidal magnetic field at the ocean bottom generated by this baroclinic ocean flow. A comparison with Fig. 3 shows that the toroidal magnetic field induced by the baroclinic flow is three orders of magnitude larger than the field generated by the barotropic flow. The induced toroidal magnetic field has the largest amplitudes in coastal regions where the horizontal ocean velocities reach large values and have a tendency to rotate, such as along the coastal regions of Argentina, Indonesia, Japan and the British Isles.

The decay of the toroidal magnetic field induced by barotropic tidal flow beneath the ocean layers for the 19-layer conductivity profile is shown in Fig. 5, where the red and blue solid lines show the real and imaginary parts of the toroidal magnetic field, respectively. We can

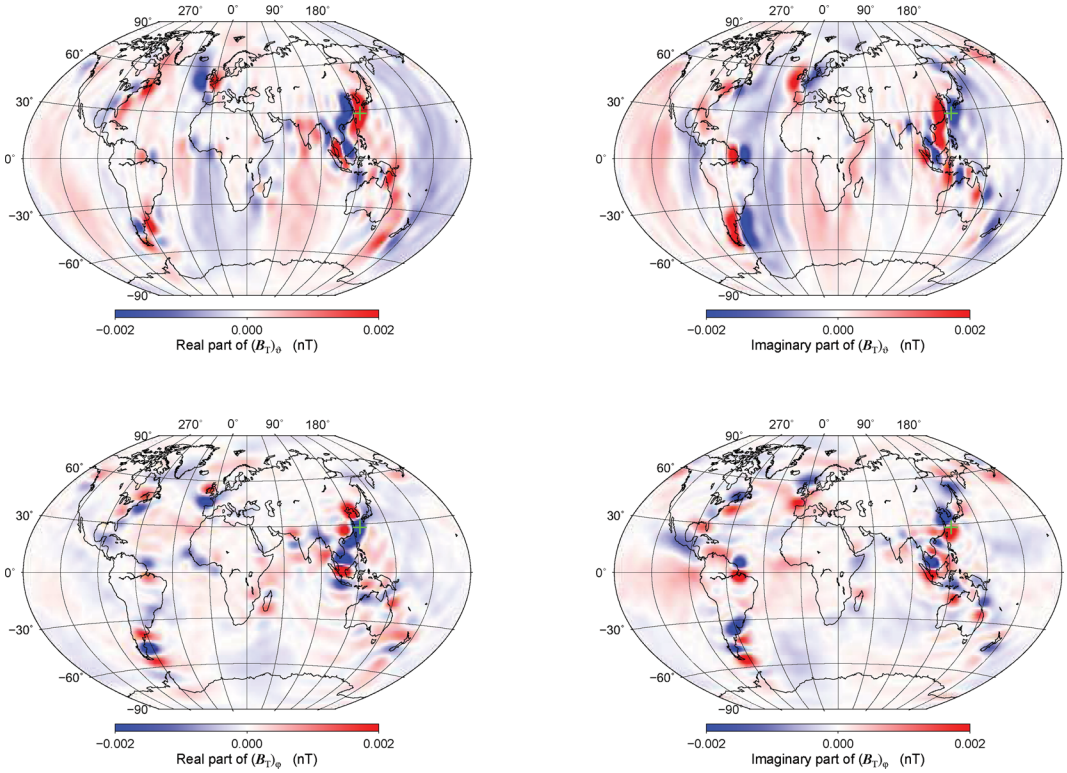

Figure 3. Real (left) and imaginary (right) parts of the ϑ (top) and φ (bottom) components of the toroidal magnetic field at the ocean bottom induced by the barotropic ocean circulation shown in Fig. 1. The green cross marks the location where the radial profile of the toroidal magnetic field is plotted (see Figs 5 and 6).

see that beneath the ocean layers where the conductivity is gradually reducing, the toroidal magnetic field decreases in amplitude down to the high resistive layer at a depth of 50 km (Fig. 2). In the underlying layer with the higher conductivity, the toroidal magnetic field decays slower, but it practically vanishes at the uppermost part of the lower mantle.

To test the sensitivity of the induced magnetic field to the conductivity structure of the crust and mantle, the equivalent magnetic field is computed for an earth model with a constant electrical conductivity of 0.1 S m^{-1} beneath the ocean layer (dashed lines in Fig. 5). Compared to the previous case, the toroidal magnetic field decays more smoothly and effectively only reaches the shallower parts of the upper mantle.

Fig. 6 shows the radial profiles of the toroidal magnetic field induced by barotropic tidal flow inside the ocean layer (marked by dark colours). The magnetic field vanishes at the sea surface, as required, and reaches its largest values at the bottom of the ocean layer for a homogeneous mantle conductivity profile (dashed lines). For a more realistic mantle conductive profile (see Fig. 2), which is effectively more resistive beneath the sedimentary layer, the toroidal magnetic field has the largest amplitudes above the ocean bottom (solid lines in Fig. 6). A general tendency is that the more resistive the underlying mantle, the more the maximum of the toroidal magnetic field is shifted towards the centre of the ocean. We can also see that the toroidal magnetic field in the ocean layer has smaller amplitudes for a realistic (i.e. more resistive) profile. In addition, to study the sensitivity of the varying electrical conductivity of the sea water on the generated toroidal magnetic field, we compare the above results (shown by the solid and dashed lines in Fig. 6) with those for a uniform sea water conductivity profile equal to 3.5 S m^{-1} (dotted lines in Fig. 6). The results show that the conductivity variations of sediments and lithosphere have a larger impact on the induced toroidal magnetic field than conductivity variations along the sea water column.

We also varied the cut-off degree j_{main} of the spherical harmonics series of the Earth main field (see eq. 14), and studied the spatial bahaviour of the induced toroidal magnetic field. For the background Earth's magnetic field $\boldsymbol{B}_0$, which is considered constant over time, we used the POMME-6 model (Maus *et al.* 2010). The dominant effect on the magnitude and the spatial pattern of the induced toroidal magnetic field has the magnetic field $\boldsymbol{B}_0$ represented by the dipole term. The shift of the magnetic poles caused by including non-dipole spherical harmonic coefficients in $\boldsymbol{B}_0$ results in minor changes in the spatial signal magnitudes, in particular the field is weakened around New Zealand. Including spherical harmonics coefficients higher than degree and order 6 has a very tiny influence on the induced magnetic field, hence the magnetic field $\boldsymbol{B}_0$ is truncated at degree and order 8 in the numerical computations.

6 SECONDARY POLOIDAL MAGNETIC FIELD

The fact that only the poloidal component of the Earth's magnetic field is observable on and outside the Earth's surface has initiated a number of theoretical studies (see Introduction Section) on the forward modelling of the ocean-induced poloidal magnetic field. Despite the toroidal component of the ocean-induced magnetic field being not directly observable outside the oceans, it couples with the large conductivity

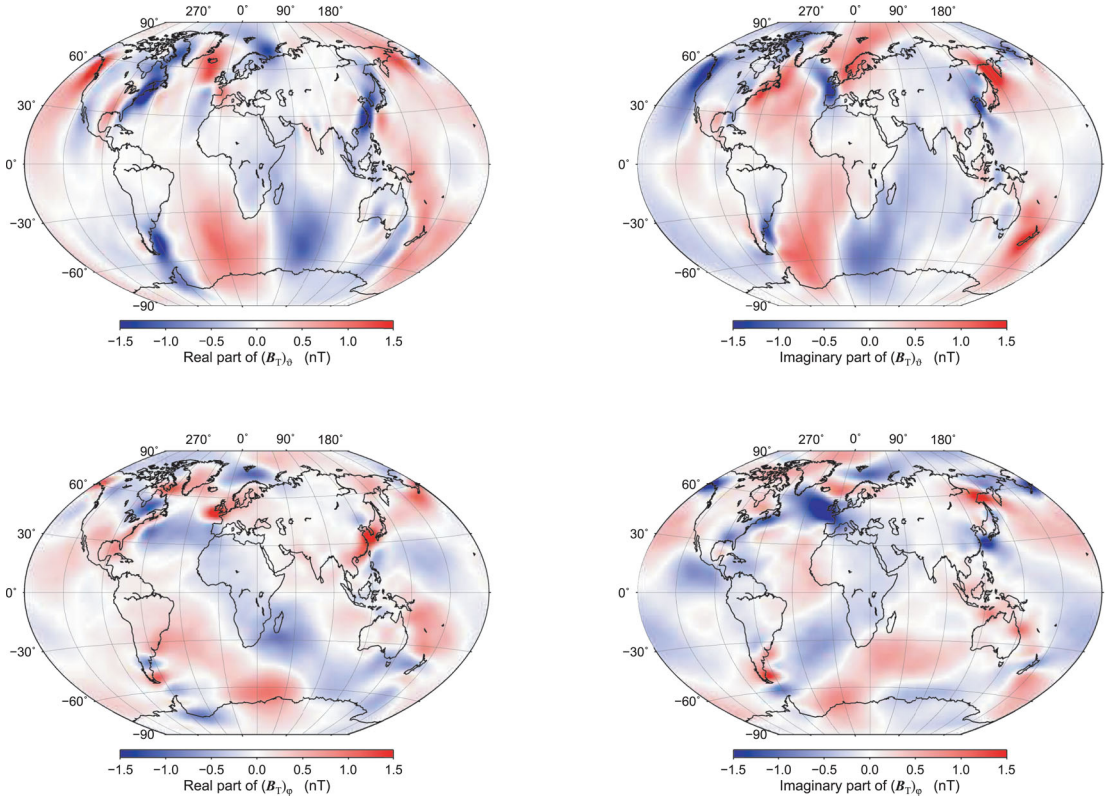

Figure 4. The same as Fig. 3, but for the baroclinic ocean circulation.

contrast between the oceans and continents and generates a secondary poloidal magnetic field of a large magnitude distributed along oceanic shorelines. Hence, in addition to the primary poloidal magnetic field, the secondary poloidal magnetic field also contributes to the geomagnetic coastal effect.

As a matter of fact, the present method does not allow a full exploitation of the mode conversion due to the coupling of the primary toroidal magnetic field with lateral heterogeneities in electrical conductivity. The following approach, thus, provides only a first estimate of the magnitude and spatial pattern of the secondary poloidal magnetic field. To make this estimate, we consider a one-layer ocean model and approximate the lateral distribution of electric conductivity in the uppermost (ocean-continent) layer by a conductivity contrast between oceans ($\sigma_o = 3.5\,\mathrm{S\,m^{-1}}$) and continents ($\sigma_c = 10^{-3}\,\mathrm{S\,m^{-1}}$). Splitting the resistivity $1/\sigma$ into radially and laterally varying parts, $1/\sigma_0$ and $1/\sigma_1$, respectively, gives

$$\frac{1}{\sigma} = \frac{1}{\sigma_0(r)} + \frac{1}{\sigma_1(\Omega)}, \tag{70}$$

while considering the spheroidal-toroidal decomposition of the magnetic induction, $\boldsymbol{B} = \boldsymbol{B}_\mathrm{S} + \boldsymbol{B}_\mathrm{T}$, the magnetic diffusion equation (2) reads as

$$\frac{1}{\mu_0}\mathrm{curl}\Big[\frac{1}{\sigma_0}\mathrm{curl}(\boldsymbol{B}_\mathrm{S} + \boldsymbol{B}_\mathrm{T})\Big] + \mathrm{curl}\Big[\frac{1}{\sigma_1}(\boldsymbol{i}_\mathrm{S} + \boldsymbol{i}_\mathrm{T})\Big] + \frac{\partial(\boldsymbol{B}_\mathrm{S} + \boldsymbol{B}_\mathrm{T})}{\partial t} = \mathrm{curl}(\boldsymbol{u} \times \boldsymbol{B}_0), \tag{71}$$

where $\boldsymbol{i}_{\mathrm{S,T}} = \mathrm{curl}\,\boldsymbol{B}_{\mathrm{T,S}}/\mu_0$ are the spheroidal and toroidal components of electrical current density, respectively. Decomposing the product of electrical current density with the lateral conductivity variations as

$$\frac{1}{\sigma_1(\Omega)}(\boldsymbol{i}_\mathrm{S} + \boldsymbol{i}_T) = \boldsymbol{j}_\mathrm{S} + \boldsymbol{j}_\mathrm{T}, \tag{72}$$

allows the induction equation to be written for the spheroidal and toroidal parts separately,

$$\frac{1}{\mu_0}\mathrm{curl}\Big(\frac{1}{\sigma_0}\mathrm{curl}\boldsymbol{B}_\mathrm{S}\Big) + \frac{\partial \boldsymbol{B}_\mathrm{S}}{\partial t} = \Big[\mathrm{curl}(\boldsymbol{u} \times \boldsymbol{B}_0)\Big]_\mathrm{T} - \mathrm{curl}\,\boldsymbol{j}_\mathrm{T}. \tag{73}$$

$$\frac{1}{\mu_0}\mathrm{curl}\Big(\frac{1}{\sigma_0}\mathrm{curl}\boldsymbol{B}_\mathrm{T}\Big) + \frac{\partial \boldsymbol{B}_\mathrm{T}}{\partial t} = \Big[\mathrm{curl}(\boldsymbol{u} \times \boldsymbol{B}_0)\Big]_\mathrm{S} - \mathrm{curl}\,\boldsymbol{j}_\mathrm{S}. \tag{74}$$

However, both equations are mutually coupled via terms $\boldsymbol{j}_{\mathrm{S,T}}$ since each of them is generated by both the spheroidal and toroidal magnetic field components. F. Vivier (personal communication, 2011) has attempted to solve the coupled system of equations by an iterative method, but he encountered numerical instabilities in an iterative solution due to the coupling terms $\boldsymbol{j}_{\mathrm{S,T}}$.

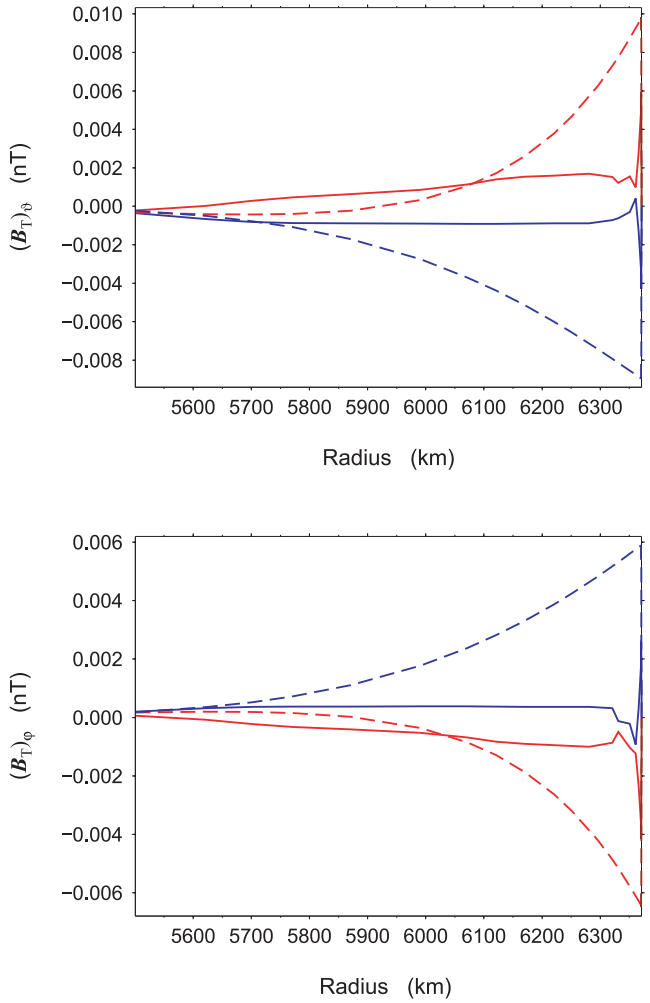

Figure 5. Real (red) and imaginary (blue) parts of the ϑ (top) and φ (bottom) components of induced toroidal magnetic field by barotropic tidal flow beneath the ocean layer for the realistic (solid lines) and uniform ($\sigma = 0.1$ S m^{-1}, dashed lines) mantle conductivity profiles, respectively. The location of the radial profile is shown by green cross in Fig. 3.

Here, we will not attempt to find a stable iterative solution of the coupled system of eqs (73) and (74), but will confine ourselves to computing the first iteration of the magnetic diffusion eq. (73) for the secondary spheroidal magnetic field $\boldsymbol{B}_S$. After solving eq. (74) with $\boldsymbol{j}_S = 0$ for the primary toroidal magnetic field $\boldsymbol{B}_T$ by applying the matrix-propagator technique developed in Section 3, the term $\boldsymbol{j}_T$ is computed by the spherical harmonic analysis of the product of the electric current density $\boldsymbol{i}$ and the lateral conductivity variations $\sigma_1(\Omega)$, as indicated by eq. (72), and substituted into magnetic diffusion eq. (73) for the secondary spheroidal magnetic field $\boldsymbol{B}_S$. This equation, solved together with the free-divergence constraint on $\boldsymbol{B}_S$ by the matrix-propagator technique designed by Pěč *et al.* (1985) yields the secondary poloidal magnetic field.

Fig. 7 shows the secondary poloidal magnetic field computed from the primary toroidal magnetic field induced by the barotropic tidal flow shown in Fig. 3. We can see that, as with the primary toroidal magnetic field, the secondary poloidal magnetic field is concentrated along the oceanic shorelines, attaining amplitudes of a few nT, comparable with the magnitudes of the primary poloidal magnetic field (Tyler *et al.* 2003; Kuvshinov & Olsen 2005; Vivier *et al.* 2004). In contrast to the primary poloidal magnetic field, the secondary poloidal magnetic field creates small-scale features concentrated in coastal regions. Note that the Gibbs phenomenon caused by the strong contrast in the conductivity between the oceans and continents has been mitigate by the Lanczos coefficients, as described in Section 4.1.

7 CONCLUSIONS AND FUTURE WORK

There is a common opinion in the geophysical community dealing with the CHAMP magnetic data that the toroidal component of the magnetic field induced by ocean circulation is larger by an order of magnitude than the induced poloidal part. This idea originated from Sanford (1971) who estimated that the toroidal magnetic field induced by ocean circulation may be as large as 100 nT. However, there are neither recent estimates, nor is there a model of the toroidal magnetic field since it is not directly observable by coastal magnetic observatories or satellite missions.

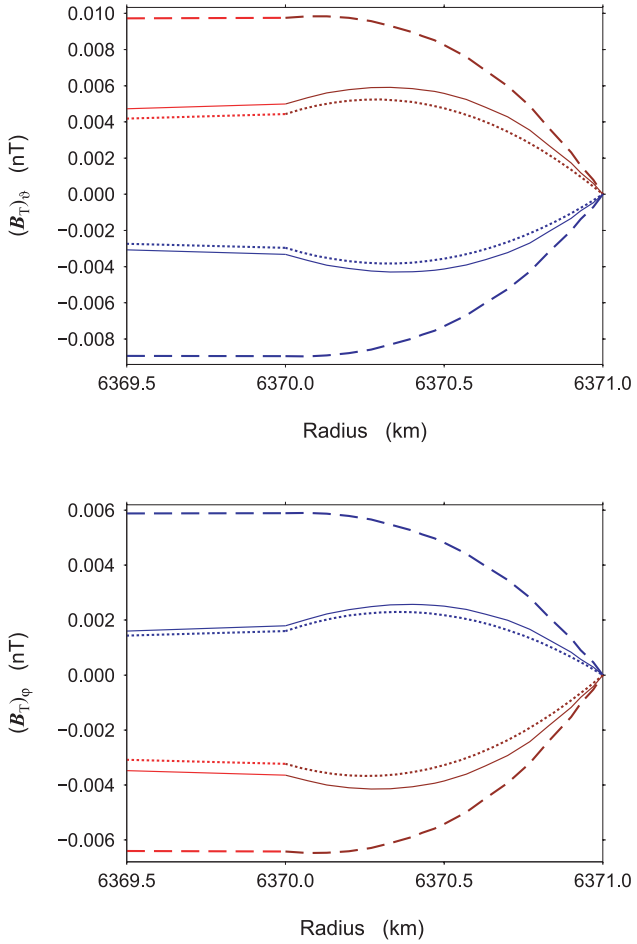

Figure 6. The same as Fig. 5, but inside the ocean layer. The dotted lines represent the case for a realistic mantle and uniform ocean ($\sigma = 3.5\,\mathrm{S\,m^{-1}}$) conductivity.

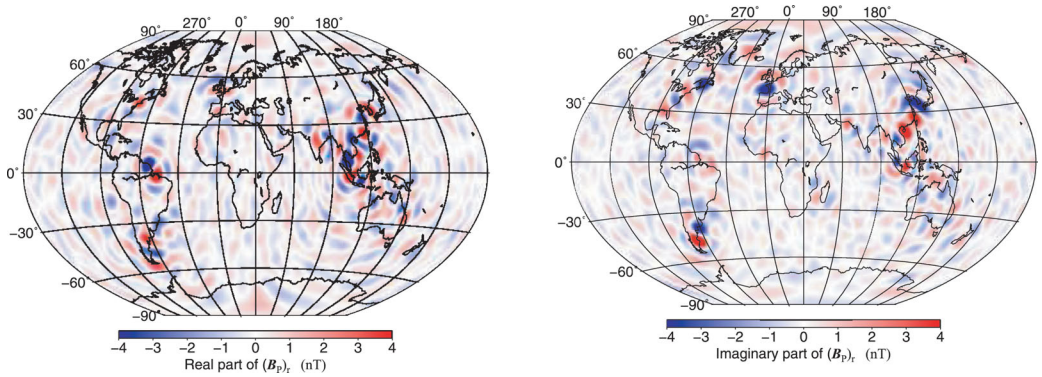

Figure 7. Estimates of the real (left-hand) and imaginary (right-hand) parts of the r component of the secondary poloidal magnetic field (coastal-effect) at the sea surface level using the toroidal magnetic field induced by barotropic flow in Fig. 3.

These two facts have motivated our study. We aimed to find a simple mathematical approach for computing a more precise estimate of the toroidal magnetic field induced by ocean flow. For the sake of simplicity, we have confined ourselves to a spherically symmetric electrical conductivity model which is exerted by a tidally induced ocean flow on the background of the main magnetic field of the Earth. Although the applied matrix-propagator technique used to compute the induced toroidal magnetic field is a mathematically appropriate tool, its numerical performance may suffer from numerical instabilities due to the necessity of computing the cross-products of the spherical Bessel functions. This causes an numerical overflow for certain setups of the model, which limits the applicability of the matrix-propagator technique.

Our numerical simulations based on the OMCT tidal ocean velocities show that the induced toroidal magnetic field is extremely sensitive to the vertical gradient of horizontal ocean flow. Depending on this gradient, the magnitudes of induced toroidal magnetic field vary from 10^{-3} nT for barotropic flow, up to several nT for baroclinic flow. Thus, the toroidal magnetic field induced by tidal ocean circulation is comparable in amplitude to the induced poloidal part (Tyler *et al.* 2003). The induced toroidal and poloidal magnetic fields differ, however,

in their spatial behaviour. Although most of the energy of the poloidal magnetic field is concentrated in large-scale spatial patterns over deep-water open oceans (Tyler *et al.* 2003; Kuvshinov & Olsen 2005), the energy associated with the toroidal magnetic field is concentrated in short-wavelength spatial patterns over shallow-water coastal regions. We should emphasize that the employed OMCT ocean velocities have a limited spatial resolution which may cause a reduction of the amplitudes of the induced toroidal magnetic field. Moreover, our results on the amplitudes of the toroidal magnetic field are valid for a tidally forced ocean circulation, whereas the estimate of 100 nT (Sanford 1971) has been done for a magnetic field induced by a general ocean circulation model. This may differ in spatial pattern, amplitude and frequency contents in comparison to tidal ocean circulation. Being explicit, we have not found a model setup for the M_2 tidal ocean flow that induces the toroidal magnetic field reaching amplitudes of 100 nT.

For laterally varying electrical conductivity, such as a continent–ocean conductivity contrast, a stable iterative method which makes use of the matrix-propagator technique should be developed. For instance, a simple iterative technique used by Zhang and Christensen (1993) for computing mantle flow due to lateral viscosity variations in the Earth's mantle can be applied to solve eqs (73)–(74) iteratively. The poloidal and toroidal components of magnetic field can still be treated separately assuming a suitable averaged radial conductivity profile $\sigma_0(r)$. The mode coupling is taken into account in an iterative way by adding $\boldsymbol{j}_{S,T}$ on the right-hand side of eqs (73)–(74). These terms arise from the deviations of the conductivity from its radial mean value and involve contributions from all other modes, which are derived from the solution of the previous iteration step. Judging from the numerical experience by Klika & Čadek (1996), this simple iterative technique would converge for a small lateral conductivity contrast not exceeding a factor of 5. However, in analogy to Klika & Čadek (1996), introducing a new variable as the product of magnetic induction and electrical resistivity may stabilize the iteration for a large conductivity contrasts. An alternative technique for solving eqs (73)–(74) could be based on an operator-splitting iterative technique. The iterations start with the matrix-propagator derived magnetic induction, which is then updated by solving an approximate problem that has more convenient numerical properties than the original setting. The convergence of the iterative algorithm which is controlled by two projection parameters, is ensured by choosing the parameters sufficiently small. Souček & Martinec (2008) applied this iterative technique on modelling of glacier flow. These ideas warrant further investigation, because a non-trivial contribution of the toroidal–poloidal mode coupled magnetic signals to the geomagnetic field at ground-based magnetic observatories situated close to the shoreline necessitates accounting for it in geomagnetic coastal-effect modelling.

ACKNOWLEDGMENTS

The authors thank Jan Hagedoorn for his scientific discussions about the problem, Kevin Fleming for his comments on the manuscript and two anonymous reviewers for their comments on the manuscript. ZM acknowledges support from the Grant Agency of the Czech Republic through Grant No. P210/10/2227.

REFERENCES

Abramowitz, M. & Stegun, I.A., 1970. *Handbook of Mathematical Functions,* Dover, New York, NY.

Baba, K., Utada, H., Goto, T., Kasaya, T., Shimizu, H. & Tada, N., 2010. Electrical conductivity imaging of the Philippine Sea upper mantle using seafloor magnetotelluric data, *Phys. Earth planet. Inter.,* **183,** 44–62.

Chave, A.D., 1983. On the theory of electromagnetic induction in the earth by ocean currents, *J. geophys. Res.,* **88,** 3531–3542.

Chave, A.D. & Luther, D.S., 1990. Low frequency, motionally induced electromagnetic fields in the ocean, 1. Theory, *J. geophys. Res.,* **95,** 7185–7200.

Colombo, O.L., 1981. Numerical methods for harmonic analysis on the sphere. Report No. 310, Department of Geodetic Science, The Ohio State University, Columbus, OH, 131pp.

Dobslaw, H. & Thomas, M., 2007. Simulation and observation of global ocean mass anomalies. *J. geophys. Res.,* **112,** C05040, doi:10.1029/2006JC004035

Duchon, C.E., 1979. Lanczos filtering in one and two dimensions, *J. appl. Meteorol.,* **18,** 1016–1022.

Klika, M. & Čadek, O., 1996. Comparison between two methods of modelling the flow in a mantle with laterally variable viscosity, *Stud. Geophys. Geod.,* **40,** 156–166.

Koch, K.-R., 1999. *Parameter Estimation and Hypothesis Testing in Linear Models,* Springer-Verlag, Berlin.

Kuvshinov, A. & Olsen, N., 2005. 3-D modelling of the magnetic fields due to ocean tidal flow, in *Earth Observation with CHAMP. Results from Three Years in Orbit,* pp. 359–366, eds Reigber, C., Lühr, H., Schwintzer, P. & Wickert, J., Springer-Verlag, Berlin.

Larsen, J.C., 1992. Transport and heat flux of the Florida Current at 27°N derived from cross-stream voltages and profiling data: theory and observations, *Phil. Trans. R. Soc. Lond., A.,* **338,** 169–236.

Lilley, F., Hitchman, A., Milligan, P.R. & Pedersen, T., 2004. Sea-surface observations of the magnetic signals of ocean swells, *Geophys. J. Int.,* **159,** 565–572.

Lizarralde, D., Chave, A.D., Hirth, G. & Schultz, A., 1995. Northeastern Pacific mantle conductivity profile from long-period magnetotelluric sounding using Hawaii to California submarine cable data, *J. geophys. Res.,* **100,** 17 837–17 854.

Manoj, C., Kuvshinov, A., Maus, S. & Lühr, H., 2006. Ocean circulation generated magnetic signals, *Earth Planets Space,* **58,** 429–437.

Maus, S. & Kuvshinov, A., 2004. Ocean tidal signals in observatory and satellite magnetic measurements, *Geophys. Res. Lett.,* **31,** 634, doi:10.1029/2004GC000.

Maus, S., Manoj, C., Rauberg, J., Michaelis, I. & Lühr, H., 2010. NOAA/NGDC candidate models for the 11th generation International Geomagnetic Reference Field and the concurrent release of the 6th generation Pomme magnetic model, *Earth Planets Space,* **62,** 729–735.

Pěč, K., Martinec, Z. & Pěčová, J., 1985. Matrix approach to the solution of electromagnetic induction in a spherically layered Earth, *Stud. Geophys. Geod.,* **29,** 139–162.

Sanford, T.B., 1971. Motionally induced electric and magnetic fields in the sea, *J. geophys. Res.,* **76,** 3476–3492.

Souček, O. & Martinec, Z., 2008. Iterative improvement of the shallow-ice approximation, *J. Glaciol.,* **54,** 812–822.

Stratton, J.A., 1941. *Electromagnetic Theory,* John Wiley, Hoboken, NJ (reissued in 2007).

Thomas, M., 2002. Ozeanisch induzierte Erdrotationsschwankungen—Ergebnisse eines Simultanmodells fuer Zirkulation und ephemeridische Gezeiten im Weltozean, *PhD thesis*, University Hamburg.

Toh, H., Satake, K., Hamazo, Y., Fujii, Y. & Goto, T., 2011. Tsunami signals from the 2006 and 2007 Kuril earthquakes detected at a seafloor geomagnetic observatory, *J. geophys. Res.,* **116,** B02104, doi:10.1029/2010JB007873.

Tyler, R.H., Mysak, L.A. & Oberhuber, J.M., 1997a. Electromagnetic fields generated by a 3-D global ocean circulation, *J. geophys. Res.,* **102,** 5531–5551.

Tyler, R.H., Sanford, T.B. & Oberhuber, J.M., 1997b. Geophysical challenges in using large-scale ocean-generated EM fields to determine the ocean flow, *J. Geomag. Geoelectr.,* **49,** 1351–1372.

Tyler, R.H., Maus, S. & Lühr, H., 2003. Satellite observations of magnetic fields due to ocean tidal flow, *Science,* **299,** 239–240.

Varshalovich, D.A., Moskalev, A.N. & Khersonskii, V.K., 1989. *Quantum Theory of Angular Momentum,* World Scientific Publications, Singapore.

Vivier, F., Maier-Reimer, E. & Tyler, R.H., 2004. Simulations of magnetic fields generated by the Antarctic Circumpolar Current at satellite altitude: can geomagnetic measurements be used to monitor the flow?, *Geophys. Res. Lett.,* **31,** doi:10.1029/2004GL019804.

Zhang, S. & Christensen, U., 1993. Some effects of lateral viscosity variations on geoid and surface velocities induced by density anomalies in the mantle, *Geophys. J. Int.,* **114,** 531–547.

APPENDIX A: SPHERICAL HARMONIC ANALYSIS OF HORIZONTAL OCEAN VELOCITIES

Let a vector field $\boldsymbol{u}$ defined on the unit sphere $(0, \pi) \times (-\pi, \pi)$ be represented as a series of vector spherical harmonics $\boldsymbol{Y}^{\ell}_{jm}(\vartheta, \varphi)$ in the form of eq. (12). To perform the spherical harmonic analysis of its values prescribed on the unit sphere, it is convenient to represent $\boldsymbol{u}$ in terms of the vector spherical harmonics $\boldsymbol{Y}^{(\lambda)}_{jm}(\vartheta, \varphi)$, $\lambda = -1, 0, 1$. The reason is that, in contrast to the vectors $\boldsymbol{Y}^{\ell}_{jm}(\vartheta, \varphi)$, the vectors $\boldsymbol{Y}^{(\lambda)}_{jm}(\vartheta, \varphi)$ are separated in orientation with respect to the r and (ϑ, φ) directions. Specifically, the vector $\boldsymbol{Y}^{(-1)}_{jm}(\vartheta, \varphi)$ is normal to the sphere surface, whereas the vectors $\boldsymbol{Y}^{(0)}_{jm}(\vartheta, \varphi)$ and $\boldsymbol{Y}^{(1)}_{jm}(\vartheta, \varphi)$ are tangential (Varshalovich *et al.* 1989),

$$\begin{aligned}
\boldsymbol{Y}^{(-1)}_{jm}(\vartheta, \varphi) &= Y_{jm}(\vartheta, \varphi)\boldsymbol{e}_{\mathrm{r}},\\
\boldsymbol{Y}^{(1)}_{jm}(\vartheta, \varphi) &= \frac{1}{\sqrt{j(j+1)}}\left[\frac{\partial Y_{jm}(\vartheta, \varphi)}{\partial \vartheta}\boldsymbol{e}_{\vartheta} + \frac{1}{\sin\vartheta}\frac{\partial Y_{jm}(\vartheta, \varphi)}{\partial \varphi}\boldsymbol{e}_{\varphi}\right],\\
\boldsymbol{Y}^{(0)}_{jm}(\vartheta, \varphi) &= \frac{i}{\sqrt{j(j+1)}}\left[\frac{1}{\sin\vartheta}\frac{\partial Y_{jm}(\vartheta, \varphi)}{\partial \varphi}\boldsymbol{e}_{\vartheta} - \frac{\partial Y_{jm}(\vartheta, \varphi)}{\partial \vartheta}\boldsymbol{e}_{\varphi}\right],
\end{aligned} \tag{A1}$$

where $Y_{jm}(\vartheta, \varphi)$ are scalar spherical harmonics and i is the imaginary unit.

In particular, a vector field $\boldsymbol{u}$ that has no radial component, such is the case for the horizontal ocean velocity field $\boldsymbol{u}$ introduced in Section 2.1, where

$$\boldsymbol{u}(\vartheta, \varphi) = u_{\vartheta}(\vartheta, \varphi)\boldsymbol{e}_{\vartheta} + u_{\varphi}(\vartheta, \varphi)\boldsymbol{e}_{\varphi}, \tag{A2}$$

and, in addition, assuming that $\boldsymbol{u}$ is a square integrable function on the unit sphere, then $\boldsymbol{u}$ can be represented in terms of $\boldsymbol{Y}^{(0)}_{jm}(\vartheta, \varphi)$ and $\boldsymbol{Y}^{(1)}_{jm}(\vartheta, \varphi)$ as

$$\boldsymbol{u}(\vartheta, \varphi) = \sum_{j=0}^{\infty}\sum_{m=-j}^{j}\sum_{\lambda=0,1} u^{(\lambda)}_{jm}\,\boldsymbol{Y}^{(\lambda)}_{jm}(\vartheta, \varphi). \tag{A3}$$

In addition, when $\boldsymbol{u}$ is a real-valued function on the unit sphere, its coefficients satisfy

$$u^{(\lambda)}_{j-m} = (-1)^{m+\lambda+1}\left(u^{(\lambda)}_{jm}\right)^{*}, \tag{A4}$$

where the asterisk stands for the complex conjugation.

The purpose of spherical harmonics analysis is to estimate two sets of coefficients $u^{(\lambda)}_{jm}$, $\lambda = 0, 1$, from the measurements of the horizontal components $u_{\vartheta}(\vartheta, \varphi)$ and $u_{\varphi}(\vartheta, \varphi)$ of $\boldsymbol{u}$ on the unit sphere. The individual samples will be called $u_{k\ell} = u_{\vartheta}(\vartheta_k, \varphi_{\ell})$ and $v_{k\ell} = u_{\varphi}(\vartheta_k, \varphi_{\ell})$. Throughout this paper, we assume that these measurements are performed over an equal angular grid where the separation between parallels, $\Delta\vartheta = \pi/N$, where N is an integer, is constant and is equal to the separation between meridians, $\Delta\varphi = \Delta\vartheta = \Delta$. For such a regular grid, data consist of values determined at the intersections of the grid and indexes k and ℓ take the values $0 \le k \le N-1$ and $0 \le \ell \le 2N-1$. Thus, there are $2N^2$ points in the equal angular grid for each component u_{ϑ} and u_{φ}, which implies that the number of fully recoverable coefficients $u^{(0)}_{jm}$ and $u^{(1)}_{jm}$ is finite. In analogy with 2-D Fourier series, Colombo (1981) has shown that the Nyquist frequency in the case of spherical harmonics is π/Δ. This implies that the maximum angular degree $j_{\max}$ up to which the coefficients $u^{(\lambda)}_{jm}$ are fully recoverable and are free of the alias effect, is given by the inequality $j_{\max} < \pi/\Delta$, or $j_{\max} < N$. As a consequence, the expansion (A3) must be replaced by a truncated spherical harmonic series,

$$\boldsymbol{u}(\vartheta, \varphi) = \sum_{j=1}^{j_{\max}}\sum_{m=-j}^{j}\sum_{\lambda=0,1} u^{(\lambda)}_{jm}\,\boldsymbol{Y}^{(\lambda)}_{jm}(\vartheta, \varphi). \tag{A5}$$

Note that the summation over j starts from $j = 1$, since $\boldsymbol{Y}^{(0)}_{00}(\vartheta, \varphi) = \boldsymbol{Y}^{(1)}_{00}(\vartheta, \varphi) = 0$ for any (ϑ, φ). In other words, $4N^2$ data are disposable for determining $j_{\max}(j_{\max}+3)$ complex harmonic coefficients $u^{(0)}_{jm}$ and $u^{(1)}_{jm}$ because of the validity of eq. (A4) for the negative-order coefficients. Estimates above the Nyquist frequency are usually regarded as meaningless. In the terminology of inverse problems, the determination of $u^{(0)}_{jm}$ and $u^{(1)}_{jm}$ is an overdetermined problem with no exact solution. In the following, the coefficients $u^{(0)}_{jm}$ and $u^{(1)}_{jm}$ will be estimated by the least-squares method.

We suppose that the data samples $u_{k\ell}$ and $v_{k\ell}$, measured over the equal angular grid,

$$\vartheta_k = \Delta/2 + k\Delta, \quad k = 0, 1, \ldots, N-1,$$
$$\varphi_\ell = \ell\Delta, \qquad \ell = 0, 1, \ldots, 2N-1, \tag{A6}$$

with $\Delta = \pi/N$, satisfy the observation equation of the form

$$\boldsymbol{y} = \boldsymbol{X}\boldsymbol{\beta} + \boldsymbol{e}, \tag{A7}$$

where $\boldsymbol{y}$ is the column vector of $4N^2$ data samples,

$$\boldsymbol{y} = [(u_{k\ell}, v_{k\ell}), k = 0, 1, \ldots, N-1, \ell = 0, 1, \ldots, 2N-1], \tag{A8}$$

$\boldsymbol{\beta}$ is the column vector of $j_{\max}(j_{\max}+3)$ coefficients $u^{(1)}_{jm}$ and $u^{(0)}_{jm}$,

$$\boldsymbol{\beta} = [(u^{(1)}_{jm}, u^{(0)}_{jm}), j = 1, \ldots, j_{\max}, m = 0, 1, \ldots, j], \tag{A9}$$

and $\boldsymbol{X}$ is the design matrix with the elements

$$X_{k\ell,jm} = \frac{1}{\sqrt{j(j+1)}} \begin{bmatrix} \dfrac{\partial Y_{jm}(\vartheta,\varphi)}{\partial\vartheta} & \dfrac{i}{\sin\vartheta}\dfrac{\partial Y_{jm}(\vartheta,\varphi)}{\partial\varphi} \\ \dfrac{1}{\sin\vartheta}\dfrac{\partial Y_{jm}(\vartheta,\varphi)}{\partial\varphi} & -i\dfrac{\partial Y_{jm}(\vartheta,\varphi)}{\partial\vartheta} \end{bmatrix}_{(\vartheta_k,\varphi_\ell)}. \tag{A10}$$

Because of data errors $\boldsymbol{e}$, eq. (A7) is mathematically inconsistent and an exact solution to this system does not exist. By assuming that errors $\boldsymbol{e}$ have zero means and are uncorrelated, the least-squares estimate $\hat{\boldsymbol{\beta}}$ of parameters $\boldsymbol{\beta}$ is given by the normal equations (e.g. Koch 1999)

$$\boldsymbol{X}^\dagger\boldsymbol{X}\,\hat{\boldsymbol{\beta}} = \boldsymbol{X}^\dagger\boldsymbol{y}, \tag{A11}$$

where the dagger stands for the conjugate transpose.

The elements of the normal matrix $\boldsymbol{X}^\dagger\boldsymbol{X}$ are

$$(\boldsymbol{X}^\dagger\boldsymbol{X})_{j_1m_1,j_2m_2} = \begin{pmatrix} B^{11}_{j_1m_1,j_2m_2} & B^{12}_{j_1m_1,j_2m_2} \\ B^{21}_{j_1m_1,j_2m_2} & B^{22}_{j_1m_1,j_2m_2} \end{pmatrix} \frac{1}{\sqrt{j_1(j_1+1)j_2(j_2+1)}} \tag{A12}$$

with the elements

$$B^{11}_{j_1m_1,j_2m_2} = \sum_{k\ell}\left[\frac{\partial\, Y^*_{j_1m_1}(\vartheta,\varphi)}{\partial\vartheta}\,\frac{\partial\, Y_{j_2m_2}(\vartheta,\varphi)}{\partial\vartheta} + \frac{1}{\sin^2\vartheta}\,\frac{\partial\, Y^*_{j_1m_1}(\vartheta,\varphi)}{\partial\varphi}\,\frac{\partial\, Y_{j_2m_2}(\vartheta,\varphi)}{\partial\varphi}\right]_{(\vartheta_k,\varphi_\ell)},$$
$$B^{12}_{j_1m_1,j_2m_2} = \sum_{k\ell}\frac{i}{\sin\vartheta}\left[\frac{\partial\, Y^*_{j_1m_1}(\vartheta,\varphi)}{\partial\vartheta}\,\frac{\partial\, Y_{j_2m_2}(\vartheta,\varphi)}{\partial\varphi} - \frac{\partial\, Y^*_{j_1m_1}(\vartheta,\varphi)}{\partial\varphi}\,\frac{\partial\, Y_{j_2m_2}(\vartheta,\varphi)}{\partial\vartheta}\right]_{(\vartheta_k,\varphi_\ell)},$$
$$B^{21}_{j_1m_1,j_2m_2} = B^{12}_{j_1m_1,j_2m_2},$$
$$B^{22}_{j_1m_1,j_2m_2} = B^{11}_{j_1m_1,j_2m_2}. \tag{A13}$$

For the equal angular grid, $\varphi_\ell = 2\pi\ell/2N$, it holds that

$$\sum_{\ell=0}^{2N-1} e^{im\varphi_\ell} = \begin{cases} 2N, & m = 0, \\ 0, & \text{otherwise.} \end{cases} \tag{A14}$$

This condition, applied to the elements of the normal matrix, eliminates the summation over longitudinal index ℓ and requires that $m_1 = m_2$,

$$B^{11}_{j_1m_1,j_2m_2} = 2N\sum_{k=0}^{N-1}\left[\frac{\partial P_{j_1m_1}(\vartheta)}{\partial\vartheta}\,\frac{\partial P_{j_2m_2}(\vartheta)}{\partial\vartheta} + \frac{m_1^2}{\sin^2\vartheta}\,P_{j_1m_1}(\vartheta)\,P_{j_2m_2}(\vartheta)\right]_{\vartheta=\vartheta_k}\delta_{m_1m_2},$$
$$B^{12}_{j_1m_1,j_2m_2} = -2Nm_1\sum_{k=0}^{N-1}\frac{1}{\sin\vartheta}\left[\frac{\partial P_{j_1m_1}(\vartheta)}{\partial\vartheta}\,P_{j_2m_1}(\vartheta) + \frac{\partial P_{j_2m_1}(\vartheta)}{\partial\vartheta}\,P_{j_1m_1}(\vartheta)\right]_{\vartheta=\vartheta_k}\delta_{m_1m_2}, \tag{A15}$$

where $\delta_{m_1m_2}$ is the Kronecker delta symbol. The last equation shows that the matrix of normal equations for the equal angular grid is sparse. To make use of it for fast numerical solutions of the normal equations, the spherical harmonic coefficients $u^{(1)}_{jm}$ and $u^{(0)}_{jm}$ are arranged in such a way that all those of the same order m are grouped together. Then, the normal matrix has a block diagonal form. For each order $m_1 > 0$, the block is of dimension $2(j_{\max} - m_1 + 1)$. The largest block is for the order $m_1 = 0$ and is of the dimension $2j_{\max}$. The smallest block is for $m_1 = j_{\max}$ and is of dimension 2×2.